Paleoseismological Constraints on the Anghiari Normal Fault (Northern Apennines, Italy) and Potential Implications for the Activity of the Altotiberina Low-Angle Normal Fault

A. Testa, P. Boncio, S. Baize, F. Mirabella, S. Pucci, B. Pace, M. Riesner, C. Pauselli, M. Ercoli, Lucilla Benedetti, et al.

▶ **To cite this version:**

A. Testa, P. Boncio, S. Baize, F. Mirabella, S. Pucci, et al.. Paleoseismological Constraints on the Anghiari Normal Fault (Northern Apennines, Italy) and Potential Implications for the Activity of the Altotiberina Low-Angle Normal Fault. Tectonics, 2023, 42 (9), pp.e2023TC007798. 10.1029/2023TC007798 . hal-04304811

HAL Id: hal-04304811
https://hal.science/hal-04304811

Submitted on 24 Nov 2023

HAL is a multi-disciplinary open access archive for the deposit and dissemination of scientific research documents, whether they are published or not. The documents may come from teaching and research institutions in France or abroad, or from public or private research centers.

L'archive ouverte pluridisciplinaire **HAL**, est destinée au dépôt et à la diffusion de documents scientifiques de niveau recherche, publiés ou non, émanant des établissements d'enseignement et de recherche français ou étrangers, des laboratoires publics ou privés.

Distributed under a Creative Commons Attribution 4.0 International License

Tectonics®

10.1029/2023TC007798

Key Points:

- Revealed the Late Pleistocene—Holocene slip history of the Anghiari fault, considered a synthetic splay of a low-angle normal fault
- The capability of the Anghiari fault to rupture the surface during $M > 6$ earthquakes has been ascertained
- The results have potential implications for the activity and seismogenic behavior of a continental low-angle normal faults

Supporting Information:

Supporting Information may be found in the online version of this article.

Correspondence to:

A. Testa,
alessio.testa@unich.it

Citation:

Testa, A., Boncio, P., Baize, S., Mirabella, F., Pucci, S., Pace, B., et al. (2023). Paleoseismological constraints on the Anghiari normal fault (Northern Apennines, Italy) and potential implications for the activity of the Altotiberina low-angle normal fault. *Tectonics*, *42*, e2023TC007798. https://doi.org/10.1029/2023TC007798

Received 8 FEB 2023
Accepted 25 AUG 2023

Author Contributions:

Conceptualization: A. Testa, P. Boncio, F. Mirabella
Data curation: A. Testa
Formal analysis: A. Testa, S. Pucci, C. Pauselli, M. Ercoli, A. Di Chiara, R. Civico
Funding acquisition: P. Boncio
Investigation: A. Testa, P. Boncio, S. Baize, F. Mirabella, S. Pucci, B. Pace, M. Riesner, C. Pauselli, M. Ercoli, A. Di Chiara, R. Civico
Project Administration: P. Boncio
Supervision: P. Boncio
Visualization: A. Testa

Paleoseismological Constraints on the Anghiari Normal Fault (Northern Apennines, Italy) and Potential Implications for the Activity of the Altotiberina Low-Angle Normal Fault

A. Testa[1], P. Boncio[1,2], S. Baize[3], F. Mirabella[4], S. Pucci[5], B. Pace[1,2], M. Riesner[6], C. Pauselli[4], M. Ercoli[4], L. Benedetti[6], A. Di Chiara[5], and R. Civico[5]

[1]Department of Engineering and Geology, Università degli Studi G. d'Annunzio Chieti e Pescara, Chieti, Italy, [2]Engineering and Geology Department, UdA-TechLab Research Center, University "G. d'Annunzio" of Chieti-Pescara, Chieti, Italy, [3]IRSN/PSE-ENV/SCAN/BERSSIN, Institut de Radioprotection et de Sureté Nucléaire, Fontenay-Aux-Roses, France, [4]Dipartimento di Fisica e Geologia, Università di Perugia, Perugia, Italy, [5]Istituto di Geofisica e Vulcanologia, Rome, Italy, [6]University of Aix Marseille, CNRS, IRD, INRAE, CEREGE, Aix-en-Provence, France

Abstract The NE-dipping Anghiari normal fault, bounding to the west the Sansepolcro basin in the Upper Tiber Valley (northern Apennines), is thought to be a synthetic splay of the Altotiberina low-angle normal fault (LANF), an active ENE-dipping extensional detachment whose seismogenic behavior is debated. In order to assess the Anghiari fault capability to break the surface during strong earthquakes and be the source of historical earthquakes, we acquired high resolution topographic data, performed field survey and geophysical investigations (Seismic reflection, Ground Penetrating Radar, Electrical Resistivity Tomography) and dug three paleoseismological trenches across different fault sections of the Anghiari fault. The acquired data reveal for the first time the Late Pleistocene to historical activity of the Anghiari fault, constraining the age of seven paleo-earthquakes over the last 25 ka, the youngest of which is comparable with one of the poorly constrained historical earthquakes of the Sansepolcro basin. The yielded slip rate is >0.2 mm/yr averaged over the last 25 ka and the recurrence interval is about 2,500–3,200 years. An analysis of the anisotropy of the magnetic susceptibility performed in one of the paleoseismological trenches revealed an extensional stress field, continuously acting during the sedimentation of the entire trenched stratigraphy. Our results confirm the ability of the Anghiari fault to generate surface faulting earthquakes. In addition, if the Anghiari fault does sole at depth into the Altotiberina low-angle normal fault, this LANF could also be seismogenic and generate $M > 6$.

Plain Language Summary We analyzed the capability of the Anghiari fault (Upper Tiber Valley, Northern Apennines of Italy) to reach and break the topographic surface during a strong earthquake. This fault may links to the Altotiberina low-angle normal fault (ATF), a detachment fault accompanied by a system of synthetic splays whose seismogenic behavior is still debated because of a lack of seismological and paleoseismological data. Thanks to geological, morphological, and geophysical analyses, four sites have been selected for paleoseismological investigation. The paleoseismological data revealed the seismic history of the Anghiari fault, assessing its capability to recurrently break the surface during strong earthquakes. In addition, an analysis of the anisotropy of the magnetic susceptibility performed in one of the paleoseismological trenches indicates that the stress field has been extensional, acting continuously during the sedimentation of the entire trenched stratigraphy. Our results suggest that the AF is capable to break the surface during strong earthquakes. This has potential implications for the seismogenic behavior of the ATF low-angle normal fault, as the strong earthquakes ($M > 6$) may nucleate on the low-angle fault plane if the AF is soling at depth into that detachment.

1. Introduction

The methodologies for assessing seismic hazard have been largely improved in the last decades thanks to the use of fault-based models, in which data deriving from earthquake geology play an important role (e.g., Field et al., 2015; Scotti et al., 2021). Compared to seismic hazard models based exclusively on historical earthquake catalogs, fault-based models have the advantage of considering periods of fault activity sufficiently long to cover several seismic cycles. This is particularly true for low-slip-rate faults, where large earthquakes can have recurrence intervals in the order of several thousand years (e.g., McCalpin, 2009). Reconstructing the slip history of active faults over multiple seismic cycles, which is a target of paleoseismic investigations in earthquake geology, is important for deriving slip rates and slip rate variabilities, which in turn are crucial for assessing the

Writing – original draft: A. Testa, P. Boncio, S. Baize, F. Mirabella, S. Pucci, B. Pace, C. Pauselli, M. Ercoli, A. Di Chiara
Writing – review & editing: A. Testa, P. Boncio, S. Baize, F. Mirabella, S. Pucci, M. Riesner, L. Benedetti

earthquake occurrence rates in seismic hazard analyses (e.g., Blumetti et al., 2017; Pace et al., 2018). In addition, near-surface characterization of active faults by paleoseismology is necessary for assessing their capability of rupturing the ground surface during earthquakes, and for estimating the associated fault displacement hazard (e.g., McCalpin, 2009; Valentini et al., 2021). However, the process of constraining active faults with paleoseismic data is slow, and in places challenging, particularly in areas where the traces of fault activity are poorly preserved because of low rates of deformation, and/or high erosion rates, and/or high anthropogenic modifications. This is the case of several active extensional basins in the Italian Apennines, where low extension rates (in the order of a few mm/yr; e.g., D'Agostino, 2014) are accommodated by low-slip-rate normal faults, often organized in parallel systems partitioning the regional deformation. Extensional basins are lowlands often occupied by urban areas and infrastructure systems, which makes those areas at high risk. In those contexts, multidisciplinary earthquake geology is a fundamental tool for evaluating seismic and fault displacement hazards.

In this paper we investigate the Sansepolcro extensional basin (Upper Tiber Valley) in the Northern Apennines of Italy. In particular, we focus on the NE-dipping Anghiari normal fault (AF), which is the northernmost part of the Anghiari-Città di Castello main fault, in the western side of the Sansepolcro basin (Figure 1). The AF is featured by evidence of recent activity as it raises Early Middle Pleistocene continental deposits in its footwall in correspondence of the Anghiari ridge. An additional point of interest is that the faults belonging to the Sansepolcro basin are thought to be synthetic and antithetic splays of the debated Altotiberina (ATF) low-angle normal fault (LANF) (Figure 1), considered as a major engine of the extension in the Upper Tiber Valley (UTV) (Boncio et al., 2000; Brozzetti et al., 2009; Chiaraluce et al., 2007; Delle Donne et al., 2007; Pucci et al., 2014). The ATF is among one of the worldwide potentially active continental LANFs (Webber et al., 2018), deserving the developments of the "Taboo" (Chiaraluce et al., 2014) Near Fault Observatory (NFO) long term research infrastructure (https://www.epos-eu.org/tcs/near-fault-observatories/about). The complex seismotectonic context of the UTV is emphasized by Brozzetti et al. (2009) who highlighted the different behavior between the northern sector, corresponding to the Sansepolcro basin, and the southern sector, corresponding to the area SSE of Città di Castello. The occurrence of strong ($M > 5.5$) earthquakes in historical times suggests that it may be possible to find geological evidence of either primary (i.e., tectonic surface ruptures) or secondary (i.e., shaking-induced features) evidence of past earthquakes (McCalpin, 2009) on the LANF or its associated structures. However, paleoseismologic studies aimed at discovering chronologically constrained field evidence of prehistoric strong surface rupturing earthquakes related to the Sansepolcro basin fault system are still missing. Only a few tectonic geomorphology and Quaternary geology studies (Benvenuti et al., 2016; Cattuto et al., 1995; Pucci et al., 2014; Sani et al., 2009), locally implemented with near-surface geophysical investigations (Delle Donne et al., 2007), are available. Since the morphotectonic expression of the Anghiari fault is pronounced, we focused on this latter fault, in order to investigate its capability to break the topographic surface during strong earthquakes. We performed detailed geological and geomorphological mapping of the Anghiari fault by means of traditional field work and digital topographic data, including high-resolution digital surface model (DSM) from satellite imagery and local very high-resolution LIDAR digital terrain model (DTM). Near-surface geophysical techniques including Seismic Reflection (SR), Ground Penetrating Radar (GPR) and Electrical Resistivity Tomography (ERT) were used to plan and accurately locate the sites for paleoseismological trenching and analysis. In this paper we will present data and evidence of recent activity on the Anghiari fault in the form of discrete, recurrent surface faulting events, that are likely associated with large earthquakes. The implications for the activity and seismogenic behavior of the Altotiberina LANF are also discussed.

2. Geological and Seismotectonic Setting

2.1. Geological Background

The Northern Apennines are a NE-verging fold-and-thrust belt resulting from the overlapping of different tectonic units during the Miocene. From west to east, the involved units are the ophiolite-bearing Ligurian unit, the Tuscan unit, and the inner and outer Umbria units (Barchi, 2010; Brozzetti et al., 2009; Pialli et al., 1998). Since the Late Pliocene, the resulting compressional structures have been superimposed by an extensional phase driven by an eastward-propagating set of low-angle detachments dipping ENE, imaged by seismic reflection profiles (e.g., CROP 03, Pialli et al., 1998). The youngest and still active fault is the ATF, a ~70 km-long structure dipping 15°–20° which bounds the western flank of the Quaternary UTV (Barchi, 2010). The ATF has accumulated up to 10 km of extension since the Pliocene (Caricchi et al., 2015; Mirabella et al., 2011). GPS data reveal 2–3 mm/yr

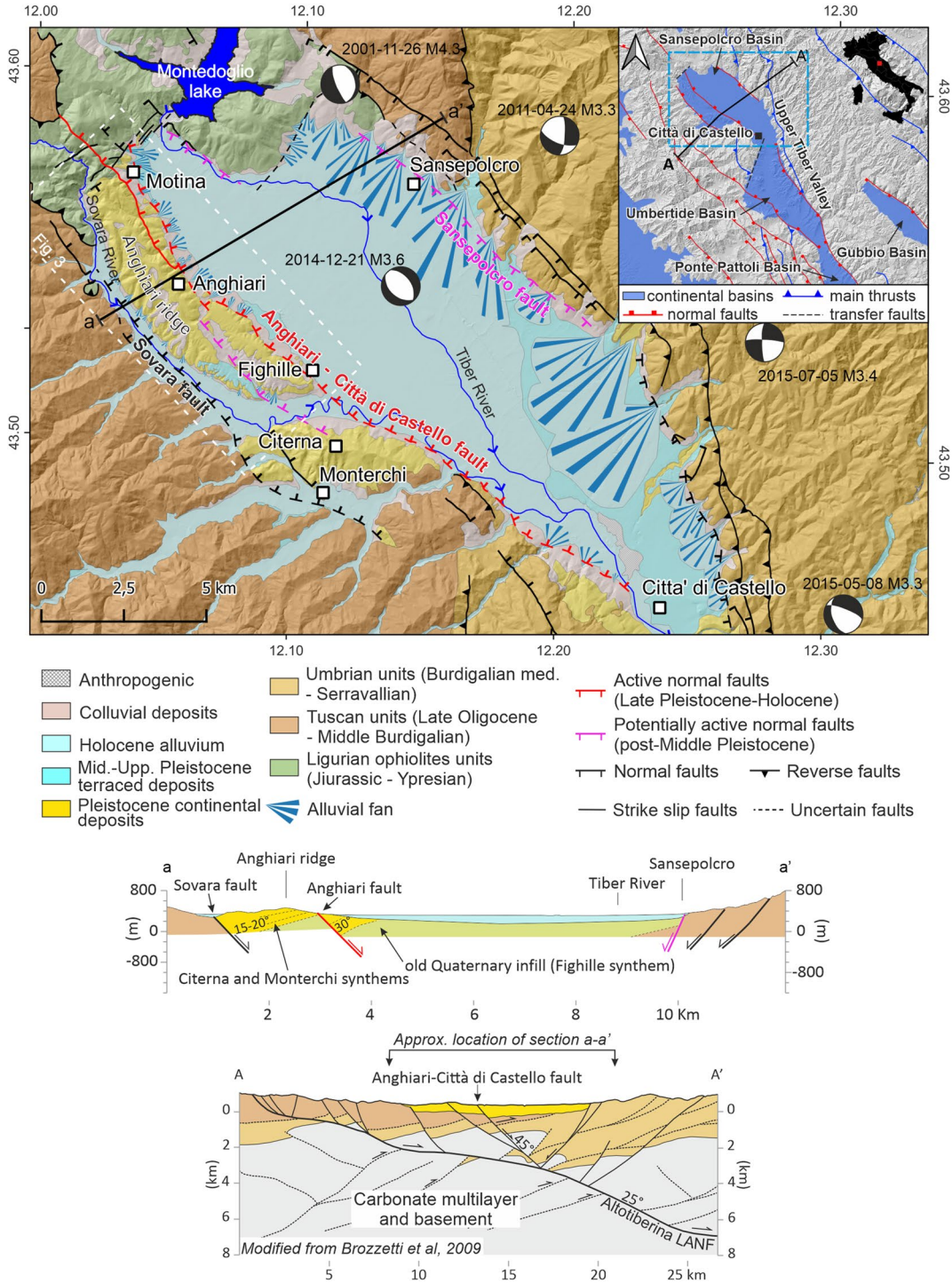

Figure 1. Simplified geological map of the Sansepolcro basin showing the main tectonic units, the distribution of the continental Pleistocene-Holocene deposits and the trace of the main faults. The faults affecting Upper Pleistocene-Holocene deposits are defined as active faults, while the faults displacing Middle Pleistocene deposits or morphologies, without more tightening age constraints, are defined as potentially active. The focal mechanisms are taken from RCMT (available at http://rcmt2.bo.ingv.it/ last access November 2022) and TDMT catalogs (available at http://terremoti.ingv.it/tdmt last access November 2022). The geological setting of the basin at shallow depth is shown in the cross-section a-a'. The regional cross-section A-A', derives from the deep seismic line CROP3 (Barchi et al., 1998a), modified from Brozzetti et al. (2009). The inset shows the location of both geological map and trace of section A-A', along with the main tectonic features and basins of the Upper Tiber Valley.

of present-day extension rate across the entire extending Apennines (Bennett et al., 2012; D'Agostino et al., 2009; Hreinsdóttir & Bennett, 2009; Mantenuto, 2008; Serpelloni et al., 2005). This is similar to the long-term geologic slip rate of the ATF (2.7 mm/yr, Mirabella et al., 2011). The most recent synthetic splays of the ATF appear to be segmented by step-over relay zones that separate three tectonically controlled Quaternary basins, the northernmost of which is the Sansepolcro basin (Figure 1), characterized by a more intense Quaternary normal fault activity, in particular along the Anghiari fault (Pucci et al., 2014).

The Sansepolcro basin is an asymmetric graben primarily controlled on the SW flank, by the NE-dipping Anghiari-Città di Castello main fault and bounded, to the NE, by a SW-dipping antithetic normal fault (Sansepolcro fault). This basin is infilled by a ∼1.0–1.2 km-thick continental succession (Barchi & Ciaccio, 2009; Mirabella et al., 2011; Pucci et al., 2014) (Figure 1).

The Sansepolcro basin exposes mainly Holocene alluvial sediments within the valley, with outcrops of Pleistocene deposits found mainly along its western side at the normal faults footwall (Figure 1). The Quaternary continental deposits are made up of fluvio-lacustrine units, unconformably covered by Middle Pleistocene to Holocene alluvial and colluvial deposits (ISPRA, 2011). The Paleo Tiber River and its western and eastern tributaries fed the Sansepolcro basin with Quaternary deposition dominated by a fluvial-lacustrine/palustrine paleo-environment. Since the Lower Pleistocene the opening of a wide extensional graben caused large infill of fine-grained sediments in the depocenter and coarse sediments along its margins. In the Middle Pleistocene the extensional activity started to exhume the Anghiari ridge, with consequent interruption of the western outflow and determining the current basin physiography (Cattuto et al., 1995). Then, the drainage of the basin was affected also by the activity of the SW-NE striking faults that bound the basin to the north, with consequent anomalies in the hydrographic network, such us fluvial deviations, of the Tiber and Sovara Rivers (Benvenuti et al., 2016; Cattuto et al., 1995; Sani et al., 2009). After the Middle Ages anthropogenic channeling shifted further east the Tiber River thalweg from the foot of the Anghiari ridge (Cattuto et al., 1995).

There are no chronologic constraints for the sedimentary units infilling the basin, therefore the unit ages and the stratigraphic frame is not univocal in the literature (e.g., Benvenuti et al., 2016; ISPRA, 2011; Pucci et al., 2014). In this paper, we follow the basic stratigraphic frame defined in the 1:50,000-scale geologic map of Italy, consisting of three Pleistocene synthems (i.e., unconformity-bounded stratigraphic units) (Fighille: FIG, Citerna: CTA, and Monterchi: MTC) covered by Middle Pleistocene to Holocene alluvial and colluvial deposits (ISPRA, 2011).

The oldest outcropping continental deposits belong to the Fighille synthem. It consists of massive or planar-laminated clay and silt, with subordinate sandy and gravelly layers, deposited in a fluvial-lacustrine/palustrine environment (i.e., periodically flooded alluvial plain, with ponds, wetlands, rare braided streams, and alluvial fans) characterized by alternating dry and humid climate. The clayey silts contain abundant plant remains, peats and lignite levels and calcareous nodules. The Fighille synthem is at least 120 m-thick (the bottom never crops out) and is tilted westward (up to 25° in the southern Anghiari ridge; Figure 1). Its deposition started before 1.8 Ma, given the mollusk assemblage and mammal faunas (late Villafranchian, Argenti, 2004; Ciangherotti & Esu, 2000; Masini & Sala, 2007).

The Citerna synthem is characterized by coarse-grained facies association, with clast-supported gravels in a sandy matrix, sand lenses and layers, clay lenses, and buried red paleosols of a braided fluvial plain environment. In the footwall of the Anghiari fault, the Citerna beds are tilted westward 15°–20°, on average, while in the hanging wall of the fault the dip can be as high as ∼30° (see section a-a' in Figure 1). The thickness of the unit is estimated in this work to be ≥150 m. Due to the absence of radiometric dating, its age is inferred to be Early Pleistocene (Pucci et al., 2014) or Middle Pleistocene (Benvenuti et al., 2016) only on the basis of stratigraphic relationships.

The Pleistocene fluvio-lacustrine sequence is closed upwards by the Anghiari sub-synthem (member of the Monterchi synthem) which is made of reddish clayey silts, fine sands, and gravel layers made of arenaceous, calcareous, and immature siliceous clasts. The thickness of the Anghiari sub-synthem is estimated in this work to be in the order of 20–25 m, and the beds are tilted westward 5°–10°. The top of this unit is highly weathered and presents stacks of paleosols with Mg-Fe-oxide nodules and carbonate nodules, suggesting an alluvial environment affected by frequent subaerial exposures during interglacial periods. Cattuto et al. (1995) suggested that the paleosol could be formed during the Mindel-Riss interglacial, but a different age cannot be excluded, as there are no chronological constraints for the age of the Anghiari sub-synthem and the overlying paleosols.

The Middle Pleistocene (upper part) to Late Pleistocene and Holocene alluvial deposits, mostly made of gravels and sands, include terraced fluvial sediments of the Sovara and Tiber Rivers and alluvial fans of variable

thickness. Their age is constrained by morpho-stratigraphic relations with the older units, by sparse radiocarbon dating and by archeological constraints (Benvenuti et al., 2016).

The deposition inside the Upper Tiber Valley has been influenced by the interaction between regional uplift and tectonic subsidence. The geological and geomorphological evidence for Quaternary activity along the UTV is concentrated within the Sansepolcro basin, where NE-dipping splays reach the surface and bound to the west the Quaternary, fluvio-lacustrine deposits (Barchi & Ciaccio, 2009; Barchi et al., 1998b; Boncio et al., 2000; Martini et al., 2001; Pucci et al., 2014; Sani et al., 2009) (Figure 1). In particular, the tectonic evidence consists of morphological fault scarps affecting the Quaternary deposits, back-tilted Pleistocene alluvial terraces and syn-tectonic sedimentary wedges that have been imaged by shallow high-resolution seismic profiles (Brozzetti et al., 2009; Cattuto et al., 1995; Delle Donne et al., 2007). According to Pucci et al. (2014), the Sansepolcro basin presents a lower vertical incision and elevated aggradation with respect to the southern basins, suggesting that the subsidence rate, controlled by the Sansepolcro basin fault system, strongly counteracts the regional uplift rate, as documented by the limited distribution of erosive forms such as fluvial terraces (see Figure 1). The main NE-dipping faults are the Sovara fault and the Anghiari—Città di Castello main fault. The Sovara fault juxtaposes the pre-continental deposits bedrock to the Pleistocene continental units, bounding the western side of the basin, along the Sovara River valley (Figure 1), and is presently buried under the Holocene alluvial deposits of the Sovara River. Present-day extension is accommodated by the Anghiari—Città di Castello main fault: it is a >20 km-long NE-dipping normal fault including two NW-SE aligned faults, the Anghiari fault to the north and the Città di Castello fault to the south, separated by the Sovara River Valley (Figure 1) (Testa et al., 2021). The average throw-rate of the Anghiari fault was inferred to be ∼0.25 mm/yr since the Middle Pleistocene, derived by the interpretation of a seismic reflection profile (Delle Donne et al., 2007), whilst 0.6–0.8 mm/yr was inferred for the Late Quaternary period based on the tilting of a fluvial terrace tread (Brozzetti et al., 2009). None of those numbers have been constrained by faulted dated markers (Figure 1).

2.2. Seismicity and Seismotectonics

Active extension across the Upper Tiber Valley is indicated by geodetic data (D'Agostino et al., 2009) and earthquake focal mechanisms (Pondrelli, 2002) (Figure 1). The area of maximum extension is concentrated across a 30–40 km-wide zone where the strongest tectonic moment is released (D'Agostino et al., 2009). The correlation between the present extensional tectonics and the activity of the NE-dipping ATF is widely agreed in the literature (e.g., Anderlini et al., 2016; Barchi et al., 1998a; Boncio et al., 2000; Chiaraluce et al., 2007; Gualandi et al., 2017; Mirabella et al., 2011; Pucci et al., 2014; Piccinini et al., 2003; Valoroso et al., 2017). Based on the distribution and characteristics of the instrumental and historical seismicity, two sectors of the ATF were identified along the UTV and east of it: the northern sector, corresponding to the Sansepolcro basin studied in this paper, and the southern sector, SSE of Città di Castello.

The southern sector is characterized by diffuse, frequent microseismicity, located along the zone around the ATF and within the ATF hanging wall, including doublets of repeating microearthquakes, aseismic slip and small-magnitude slow-slip events (Chiaraluce et al., 2007; Gualandi et al., 2017; Piccinini et al., 2003; Valoroso et al., 2017). Here, the most energetic earthquakes are expected to be released by SW-dipping, NW-SE-striking antithetic normal faults (e.g., the Gubbio normal fault, Mirabella et al., 2004; Pace et al., 2006) (Figure 1). The northern sector, that is, the Sansepolcro basin, is characterized by much lower microseismicity activity, compared to its southern counterpart, and was struck by several destructive historical earthquakes (Figure 2). This has been interpreted as the evidence that this segment is locked (Brozzetti et al., 2009), and supposedly slips during moderate to large earthquakes that nucleate at shallow depths on steeper ramps (25°–30°) of the ATF and/or on high-angle synthetic splays. In particular, the ATF ramp at 3–7 km-depth and its continuation up to the surface along the Anghiari fault (see section A-A' in Figure 1) has been considered as the major potential seismogenic source of the area (named Città di Castello in Brozzetti et al. (2009)).

A dense network of GPS data, yield ∼2–2.5 mm/yr of extension driven by the ATF, mostly accommodated with creep below depths of 4–5 km (Anderlini et al., 2016; Hreinsdóttir & Bennett, 2009). The modeled geodetic strain (Anderlini et al., 2016) suggests that the ATF is mainly locked down to 4–5 km of depth, whereas creeps at a rate of 1.7 ± 0.3 mm/yr between 4–5 and 7 km, with a deep locked patch between 7 and 10 km. According to Anderlini et al. (2016), one of the main shallow locked patches is in the Sansepolcro basin. The main creeping portion correlates well with the area of intense microseismicity SSE of Città di Castello. Such a fault architecture

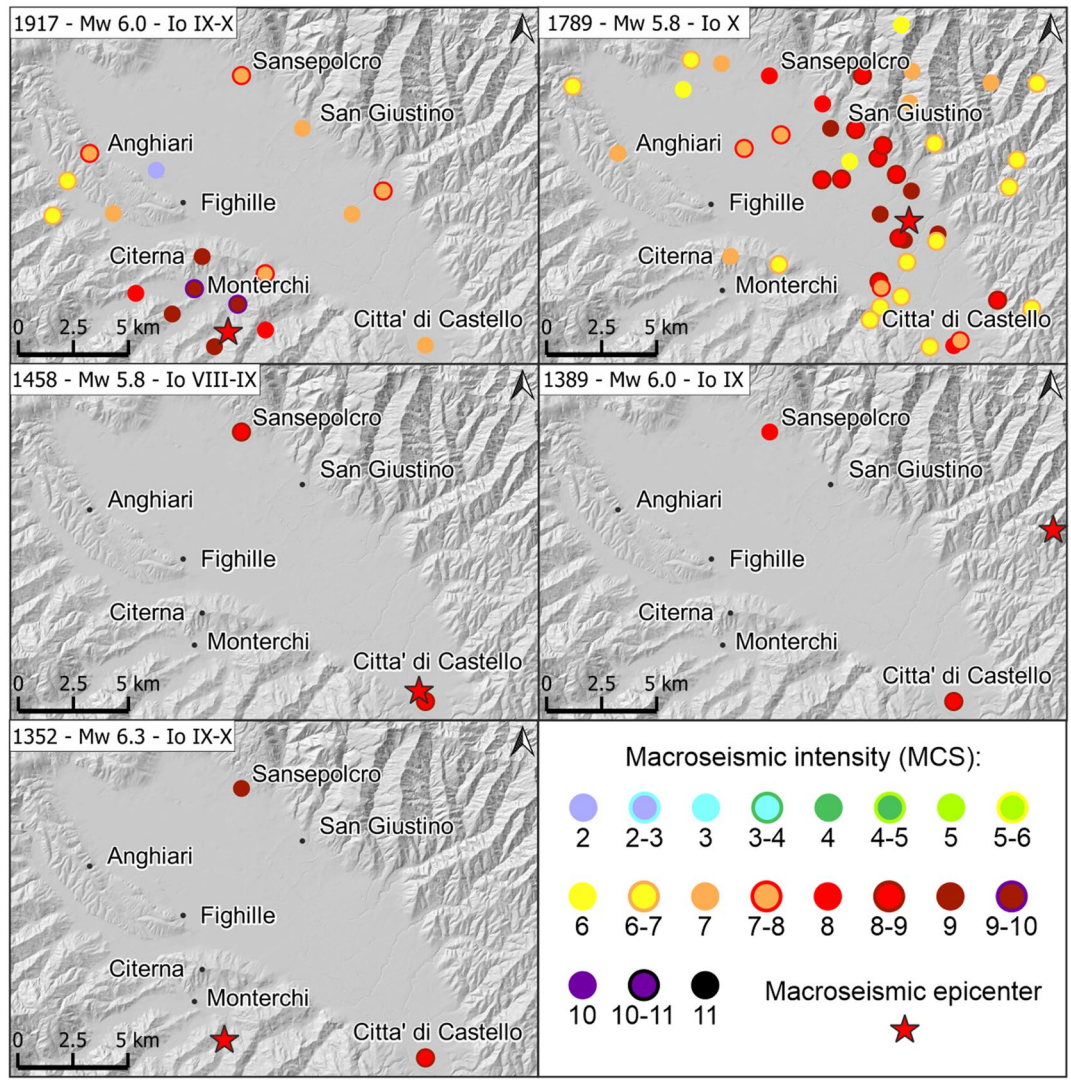

Figure 2. Distribution of the macroseismic intensities related to the main historical earthquakes ($M_w \geq 5.5$) occurred in the Sansepolcro basin. In detail the following events are represented in order: 1917 (M_w 6.0, Mercalli Cancani Sieberg macroseismic intensity I_0 IX-X); 1789 (M_w 5.8, I_0 X); 1458 (M_w 5.8, I_0 VIII-IX); 1389 (M_w 6.0, I_0 IX); and h) 1352 (M_w 6.3,I_0 IX-X) (Rovida et al., 2022).

and slip behavior produce a positive stress build up on the shallow locked portion of the ATF, and on most of the hanging wall splays, including the Anghiari fault. Based on the size and strain rate of the inferred locked patches, Anderlini et al. (2016) estimated a seismic potential of the ATF up to Mw 6.5–6.7 over a time interval of 10^3 years. On the other hand, seismic slip-on hanging wall splays might favor potential seismic slip or transient acceleration of creep on deeper portions of the ATF.

Figure 2 shows the epicentral macroseismic intensities of the earthquakes that hit the Sansepolcro basin in the past centuries. The main events ($M_w \geq 5.5$) are the 1352 (M_w 6.3, Mercalli-Cancani-Sieberg macroseismic intensity - I_0 - IX-X), 1389 (M_w 6.0, I_0 IX), 1458 (M_w 5.8, I_0 VIII-IX), 1789 (M_w 5.8, I_0 X), 1917 (M_w 6.0, I_0 IX-X) earthquakes (Rovida et al., 2022). Other significant events ($5 \leq M_w \geq 5.5$) are the 1489 (M_w 5.1, I_0 VII), 1558 (M_w 5.1, I_0 VII), and 1919 (M_w 5.0, I_0 VI) earthquakes (Rovida et al., 2022). Based on the distribution of the intensity data points, Brozzetti et al. (2009) proposed that the 1389, 1458, and 1789 could have nucleated on the southern sector of the Anghiari-Città di Castello main fault, while the 1917 Monterchi earthquake could have nucleated on a western and shallower synthetic splay of the ATF. Similarly, as possible evidence of NE-dipping source of the 1917 earthquake, Delle Donne et al. (2007) consider as primary surface faulting the ~1 km-long,

NW-SE-striking coseismic ground failure occurred near Monterchi and described by Oddone (1918) (although the latter did not exclude its landslide genesis). A different interpretation of the 1917 earthquake is proposed by Caciagli et al. (2019), who reanalyzed instrumental historical data and calculated a relatively deep hypocentral location (~8 ± 4 km-depth), a relatively high magnitude (Mw 5.8) and a first-arrival focal solution. The most plausible solution proposed by these authors is a NE-striking right-lateral strike-slip fault in the footwall of the ATF, possibly related to a transfer fault responsible for the segmentation of the ATF.

None of the seismotectonic interpretations mentioned above is constrained by paleoseismological evidence in historical or Holocene layers that might prove the activity of the fault(s) up to the surface. In this paper we present constraints on the Late Pleistocene and Holocene activity of the Anghiari fault.

3. Methods

3.1. Field and Remote Sensing Surveys

Field investigations and geological and geomorphological mapping were carried out along the eastern side of the Anghiari ridge in order to map the surface trace of the Anghiari fault as well as to identify faulted stratigraphic and topographic markers constraining the fault slip history and slip rate. Most of the geologic and geomorphic features such as fault traces and the contacts of Quaternary geological bodies were identified integrating both conventional field mapping and remote sensing techniques: the former was performed using a field tablet integrating a commercial GPS device and a dedicated digital mapping suite (Field Move Software Suite, Petroleum Experts); the latter included the acquisition and analysis of LiDAR data, airborne-acquired through a Riegl miniVUX Sys DL laser scanner mounted on a DJI Matrice 600 pro drone. This acquisition produced a dense point cloud (300 pts/m^2) from which a very high-resolution Digital Terrain Model (DTM) (0.2-m pixel size) of 1.45 $km^2$was built. Then, the derivatives shaded relief, slope and aspect maps, were jointly and carefully analyzed (Figure 4). Moreover, at the scale of the Sansepolcro basin we used the 10 m resolution TINITALY Digital Elevation Model (DEM) (Tarquini et al., 2012) and a newly acquired Digital Surface Model (DSM) derived from stereo pairs of Pleiades satellite optical images (50 cm resolution).

3.2. Geophysical Investigations (GPR, Seismic, ERT)

Following the field and geomorphological mapping, we carried out a geophysical campaign aimed at determining the most accurate position of the fault traces which could be the target for paleoseismological trenching. Across some sites with morphological fault expressions, we have used/combined high-resolution seismic reflection (SR), ground-penetrating radar (GPR), and electrical resistivity tomography (ERT) acquisitions. We present the results achieved combining high-resolution SR and GPR at the Villa Sterpeto site (location in Figures 3 and 4) and the ERT at the Anghiari site A (location in Figure 4), surveyed at the paleoseismological trench floor.

The SR profile was 167 m-long, ~58°N oriented, and acquired across the scarp between the slope made of Citerna synthem and the paleo-surface curved on the Anghiari sub-synthem.

A 24-bit DoReMi seismograph, manufactured by SARA Electronic Instruments (https://www.sara.pg.it) and equipped with 72 channels linked to vertical geophones (40 Hz), and a sledgehammer source of 8 kg was used for the acquisition of *P*-waves. The geophone spacing was set up to 1 m and thus 0.5 m was the CDP spacing. In addiction we obtained a seismic tomography velocity model. To increase the resolution along the near surface portion of the seismic section, a GPR profile 62 m-long and ~67°N oriented was collected crossing the possible fault trace, aiming to better constrain the fault geometry at shallow depth. The GPR line was recorded using a Zond-12e GPR system, equipped with a 100 MHz antenna (Tx and Rx), using a survey wheel and Topcon GR-5 GNSS device in NRTK configuration, to record the coordinates and elevation of each trace. Despite the clear high conductivity of the soil at the study site, limiting the probing depth to ~2 m, the processed GPR profile shows an improved image of the shallow geometries. The processed SEG-Y files were finally imported in the seismic interpretation software OpendTect Pro v.6.4 (academic license courtesy of dGB Earth Science, https://www.dgbes.com, last access: 3 January 2023) for an enhanced display obtained by the calculation of selected seismic attributes (Taner et al., 1979) computed on the GPR signal amplitude and phase, already proven to be effective for detecting fractures and faults (Ercoli et al., 2015; Forte et al., 2012). In particular, the instantaneous phase (Cinti et al., 2015) enhances the interpretability of the reflections geometry and the enhancement of lateral

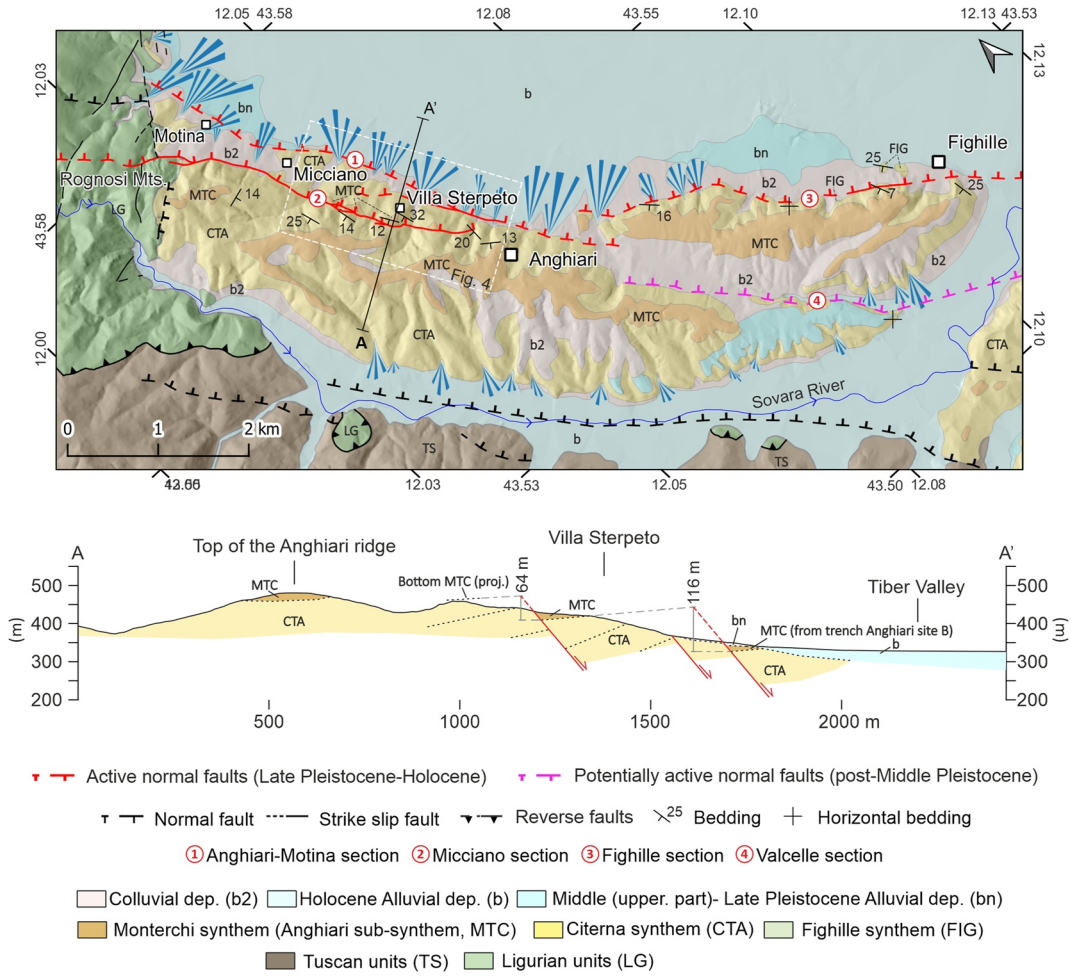

Figure 3. Detailed geological map of the Anghiari ridge showing the distribution of the main geologic units and the segmentation of the Anghiari fault, based on ISPRA (2011) and integrated with original field survey. The measured displacement of each segment of the Anghiari fault is shown in the geologic cross section A-A' (no vertical exaggeration). Dashed lines indicate buried or inferred fault traces. See the caption of Figure 1 for the definition of active and potentially active faults. The white dashed square indicates the location of the map in Figure 4.

discontinuities. Being independent on the reflection strength, this attribute is also effective in strongly attenuated areas characterized by weak reflectivity (Ercoli et al., 2021a), thus propaedeutic for ground truthing. The latter aids not only the stratigraphic interpretation but also enhances lateral geophysical discontinuities associable to shallow fracturing and/or faulting.

A MAE XM612EM+ equipment has been used to acquire an ERT profile along the floor of the trench Anghiari site A, with a maximum electric voltage of 200V and a minimum electricity of 150 mA. The resulting resistivity profile has a maximum depth of 7–8 m and a spatial resolution of 0.5.

Further details about the acquisition and processing of the geophysical analysis are given in Text S1 in Supporting Information S1.

3.3. Paleoseismological Trenching

The paleoseismological investigations were conducted between winter 2021 and summer 2022 in two sites across the Micciano fault section (Villa Sterpeto, Podere Todari sites) and two sites across the supposed trace of the Anghiari-Motina fault section (Anghiari sites A and B) (Figure 4). First we dug by backhoe a semi-benched trench, 60°-trending, 50 m-long and 3 m-deep at the Villa Sterpeto site, across the fault trace highlighted by the high-resolution SR and GPR data interpretation.

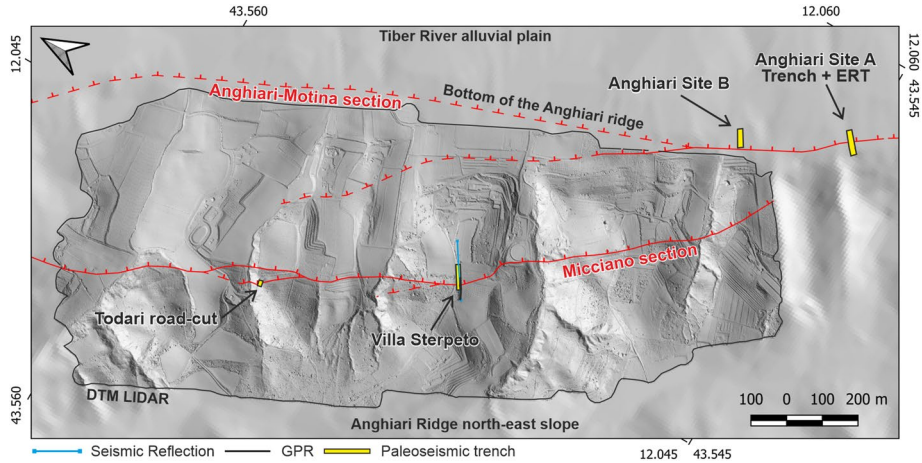

Figure 4. Location map of the geophysical investigations and Paleoseismological trenches. The topographic maps are the 10 m/pixel DTM TINITALY (Tarquini et al., 2012) and the newly acquired, 0.2 m/pixel DTM LIDAR. The traces of the Anghiari-Motina and Micciano fault sections are shown in red.

At the Podere Todari site, we widened and rectified by backhoe a pre-existing, 80°-trending anthropogenic road-cut exposing faulted colluvial deposits across a synthetic splay of the Micciano fault section. The wall of the rectified roadcut was 7 m-long and 2.5 m-high. Finally, we dug two trenches by backhoe at the Anghiari sites A and B across the supposed trace of the Anghiari-Motina fault section. The trench of site A was 50°-trending, 55 m-long, 3 to 4 m-deep, with a benched layout. The trench of site B was 60°-trending, 40 m-long, 3 m-deep, with a benched layout. The location of the trench Anghiari Site A was chosen based on an outcrop of the Citerna synthem at the base of the scarp below the road S.P. 47 suggesting that the scarp is in the footwall of the fault and that the fault is located a few meters downslope. The location of the trench Anghiari site B would have to cross the supposed trace of the Anghiari-Motina fault section in order to compensate for the lack of unequivocal evidence in the site A. However, this trench is completely located within the hanging wall of the fault.

In all the four sites, the trench walls were accurately smoothed and cleaned. The faults and the main stratigraphic contacts were identified, flagged with colored pins, and logged. Wall logs were drawn at 1:50 scale for Villa Sterpeto and Anghiari sites and 1:20 scale for Podere Todari site. As a basis for the wall logs, four orthophotomosaics were generated from ground-based 24-megapixel imagery, acquired using a Canon 850d camera, and processed by structure-from-motion photogrammetry through Agisoft Metashape®. High-resolution orthophotomosaics are reported in Figures S1–S4 in Supporting Information S1.

3.4. Sample and Events Dating

We collected 18 samples from paleoseismological trenches for radiocarbon dating, 8 at the Villa Sterpeto, 6 at the Todari, and 4 at the Anghiari A sites. Charcoal was found and dated in 3 samples (Anghiari site A), the other samples consist of organic sediment, for which we dated the bulk organic fraction. The radiocarbon dating was performed with accelerator mass spectrometry technique in the laboratories of Beta Analytic for 13 samples (https://www.radiocarbon.com/, last access: 26 August 2022) and in the Laboratory Plateforme Nationale LMC14, France (http://lmc14.lsce.ipsl.fr/, last access: 21 March 2022), for 5 samples (complete list of the samples and samples age in Table 1). The uncalibrated ages given from the LMC14 laboratory were calibrated by us using the IntCal20 atmospheric calibration model (Reimer et al., 2020) in OxCal. The original reports of the dating, and the results of the calibration (referring to the samples dated in the Laboratory Plateforme Nationale LMC14) are reported in the additional Supporting Information S1. The age of six pottery shards collected in the Anghiari site A trench was estimated by O. Menozzi, archeological expert of the University of Chieti—Pescara (personal communication). The dated samples allowed us to constrain the age of the stratigraphy and the bracketing ages of the surface faulting earthquakes. In order to refine the earthquakes chronology we used the Boundary-Zero Boundary model in OxCal v4.4.4 (Bronk Ramsey, 1995, 2008, 2009; atmospheric calibration model by Reimer et al., 2020). Based on provided dating constraints (i.e., radiocarbon dating), this approach uses Bayesian probability to obtain probability density functions of the events, forcing the model to skew the age based

Tectonics

10.1029/2023TC007798

Table 1
Summary of Radiocarbon Dating Analysis

Sample name	Longitude (°E)	Latitude (°N)	Trench name	Depositional unit	Material (dated material)	Method—lab.	Date of sampling (dd/mm/yyyy)	Conventional radiocarbon age BP	Calendar calibrated results (%)
VS_C01	12.0459	43.5521	Villa Sterpeto	6	Organic sediment (bulk organic fraction)	AMS—Beta Analytic	18/11/2021	20,600 ± 70 BP	23,126–22,626 BCE (95.4%)
VS_C02	12.0459	43.5521	Villa Sterpeto	5	Organic sediment (bulk organic fraction)	AMS—Plateforme Nationale LMC14	18/11/2021	13,210 ± 60 BP	14,106–137,17 BCE (95.4%)
VS_C03	12.0459	43.5521	Villa Sterpeto	5	Organic sediment (bulk organic fraction)	AMS—Plateforme Nationale LMC14	18/11/2021	14,330 ± 70 BP	15,863–15,321 BCE (91.2%) 15,286–15,198 BCE (4.3%)
VS_C06bis	12.0459	43.5521	Villa Sterpeto	3	Organic sediment (bulk organic fraction)	AMS—Plateforme Nationale LMC14	18/11/2021	5,650 ± 35 BP	4,551–4,436 BCE (78.5%) 4,430–4,363 BCE (16.9%)
VS_C07	12.0459	43.5521	Villa Sterpeto	Fz1	Organic sediment (bulk organic fraction)	AMS—Plateforme Nationale LMC14	01/12/2021	1,990 ± 30 BP	46–85 CE (88.2%) 95–117 CE (7.3%)
VS_C08	12.0459	43.5521	Villa Sterpeto	Fz1	Organic sediment (bulk organic fraction)	AMS—Plateforme Nationale LMC14	01/12/2021	5,330 ± 30 BP	4,315–4,300 BCE (3.1%) 4,252–4,151 BCE (45.4%) 4,145–4,050 BCE (47%)
VS_C12	12.0459	43.5521	Villa Sterpeto	5	Organic sediment (bulk organic fraction)	AMS—Beta Analytic	01/12/2021	11,910 ± 40 BP	11,864–11,656 BCE (82%) 12,054–11,991 BCE (10.7%) 11,908–11,882 BCE (2.7%)
VS_C13	12.0459	43.5521	Villa Sterpeto	5	Organic sediment (bulk organic fraction)	AMS—Beta Analytic	01/12/2021	12,940 ± 40 BP	13,677–13,351 BCE (95.4%)
Tod_C01	12.0421	43.5564	Todari Roadcut	6	Organic sediment (bulk organic fraction)	AMS—Beta Analytic	19/11/2021	6,270 ± 30 BP	5,318–5,207 BCE (91%) 5,162–5,125 BCE (4%) 5,089–5,084 BCE (0.4%)
Tod_C02	12.0421	43.5564	Todari Roadcut	5	Organic sediment (bulk organic fraction)	AMS—Beta Analytic	19/11/2021	4,710 ± 30 BP	3,468–3,373 BCE (54.8%) 3,534–3,489 BCE (24.1%) 3,626–3,576 BCE (14.9%) 3,571–3,561 BCE (1.6%)

Tectonics

10.1029/2023TC007798

Table 1
Continued

Sample name	Longitude (°E)	Latitude (°N)	Trench name	Depositional unit	Material (dated material)	Method—lab.	Date of sampling (dd/mm/yyyy)	Conventional radiocarbon age BP	Calendar calibrated results (%)
Tod_C03	12.0421	43.5564	Todari Roadcut	5	Organic sediment (bulk organic fraction)	AMS—Beta Analytic	19/11/2021	2,730 ± 30 BP	928–810 BCE (95.4%)
Tod_C04	12.0421	43.5564	Todari Roadcut	2	Organic sediment (bulk organic fraction)	AMS—Beta Analytic	19/11/2021	300 ± 30 BP	1,495–1,602 CE (69.3%) 1,610–1,656 CE (26.1%)
Tod_C05	12.0421	43.5564	Todari Roadcut	FF	Organic sediment (bulk organic fraction)	AMS—Beta Analytic	19/11/2021	470 ± 30 BP	1,408–1,460 CE (95.4%)
Tod_C06	12.0421	43.5564	Todari Roadcut	4	Organic sediment (bulk organic fraction)	AMS—Beta Analytic	14/07/2022	1,260 ± 30 BP	668–776 CE (73.9%)
TA_C3	125.452	43.5420	Anghiari site A	4b	Charcoal (charred material)	AMS—Beta Analytic	08/07/2022	4,350 ± 30 BP	3,027–2,899 BCE (92.8%) 3,076–3,064 BCE (2.6%)
TA_C6	12.0568	43.5452	Anghiari site A	3a	Charcoal (charred material)	AMS—Beta Analytic	08/07/2022	1,450 ± 30 BP	571–651 CE (95.4%)
TA_C8	12.0568	43.5452	Anghiari site A	4b	Charcoal (charred material)	AMS—Beta Analytic	08/07/2022	4,500 ± 30 BP	3,351–3,096 BCE (95.4%)

on geological evidence interpreted as developed immediately before (i.e., earthquake horizons) or immediately after (colluvial wedges) the earthquakes. Therefore, the earthquake ages computed using OxCal are narrower than the time windows between each couple of samples, and the probability density function has a skewness through the sample that, according to our interpretation, fits much better with the age of the events.

3.5. Anisotropy of Magnetic Susceptibility

The anisotropy of magnetic susceptibility (AMS) can be used as a proxy for rock fabrics (Borradaile, 1988; Borradaile & Henry, 1997; Borradaile & Jackson, 2004; Hrouda, 1982; Tarling & Hrouda, 1993), reflecting the preferred orientation of grains, grain distributions and/or the crystal lattices of minerals that contribute to the magnetic susceptibility of a rock (e.g., Borradaile & Jackson, 2004; Tarling & Hrouda, 1993).

In particular, AMS is extremely sensitive to incipient strain in fine-grained sediments well before other macro and mesoscopic strain features (such as cleavage) can be observed in the field. In general, in compressive tectonic settings, the magnetic lineation (the maximum susceptibility axis) is commonly parallel to fold axes and thrust faults, while in extensional regimes, it is perpendicular to normal faults and parallel to bedding dip directions (e.g., Borradaile & Jackson, 2004; Maffione et al., 2012).

In order to understand the relations between these units and the fault activity, the anisotropy of the magnetic susceptibility (AMS) of clay layers, the paleosol and the colluvial deposits was investigated in the Villa Sterpeto trench. Eight blocks were collected using a Bosch Professional 18V System GOP multitool. Each block was oriented with a Brunton magnetic compass and extracted, numbered from 1 to 8, where the latter is the closest to the fault in the Villa Sterpeto trench. Blocks ANG01 to 05 were collected in clays, ANG06 and 07 on the paleosol and ANG08 on the colluvial deposits. From each block, 5 to 8 oriented ~1.5 cm^3 cubes were cut using a diamagnetic saw, in the rock preparation laboratory at INGV, Rome. For each of the 50 samples, the bulk susceptibility and the low field AMS was measured on all samples on a AGICO KLY 3S Kappabridge and the results were processed using the AGICO software Anisoft (https://www.agico.com/text/software/anisoft/anisoft.php). Further information about this methodology is given in Text S2 in Supporting Information S1.

4. Results

4.1. Anghiari Fault From Geological and Geomorphological Mapping

The Anghiari normal fault is characterized by a segmented pattern in map view, formed by at least four fault sections, namely the Anghiari-Motina, Micciano, Fighille and Valcelle sections (1, 2, 3, and 4, respectively, in Figure 3).

The 5.5 km-long Anghiari-Motina section bounds the eastern side of the Anghiari ridge, separating the Citerna synthem (CTA) in the footwall from the Holocene colluvial and alluvial deposits in the hanging wall. The fault trace is barely visible in the field and is often concealed by anthropogenic modifications. Its trace was mapped using first-order morphological evidence, such as escarpments on the CTA sediments uplifted in its footwall block, and the alignment of apexes of the youngest generation of alluvial fans developing in its hanging wall. The fault location is further constrained by data acquired within trenches A and B near Anghiari. The average strike of the Anghiari-Motina section is N150. A 1.5 km-long, WNW-striking secondary splay (Figure 4), crossed by the geologic section in Figure 3, branches out from the principal fault trace and displaces some paleosurfaces located between the Anghiari-Motina and Micciano fault sections.

The 6 km-long Micciano section runs within the Anghiari ridge, from the Rognosi Mts. to the northern part of the Anghiari town. In its northern sector, the fault separates the Meso-Cenozoic bedrock (Ligurian units) from the Lower-Middle Pleistocene CTA unit and then continues to the NW within the bedrock. The fault is characterized by prominent morphotectonic evidence, such as triangular facets, deeply incised gullies, and down thrown paleosurfaces (See Figure 4 for details). The average strike of the Micciano section is N145.

The 4.8 km-long Fighille section runs at the base of the Anghiari ridge, from the southern part of the Anghiari town to the Sovara River valley. A left step-over separates this section from the Anghiari-Motina section. As first-order geomorphic evidence, the fault separates the Lower-Middle Pleistocene CTA sediments of the Anghiari ridge from the Tiber River alluvial plain. At a closer view, the fault trace is often concealed by anthropogenic

modifications and its trace can be inferred thanks to aligned escarpments on the CTA sediments and the alignment of the youngest generation of alluvial fans in the hanging wall. The average strike of the Fighille fault section is N130.

The 5 km-long Valcelle fault section is located within a NW-SE-oriented valley that crosses the Anghiari ridge, from the Anghiari town to the southern side of the Sovara River valley. It is confined within the CTA synthem, without prominent geomorphic expression, except for the southern part, where the fault crosses the Sovara River and forms a straight scarp within the CTA synthem, on the southern side of the valley (Figure 1). The average strike of the Valcelle fault section is N130. This fault section is described as only potentially active in Figure 3 since it only affects Early Middle Pleistocene deposits.

The geologic section A-A' in Figure 3 crosses orthogonally both the Micciano and Anghiari-Motina fault sections, showing a throw component of 64–116 m of the MTC bottom, respectively.

4.2. Villa Sterpeto Site

The following sections illustrate the results of both geophysical and paleoseismological investigations conducted at Villa Sterpeto

4.2.1. Geophysics

The seismic reflection profile reveals two high amplitude, low frequency reflections, due to a strong acoustic impedance contrast, gently dipping toward east and located between 15 and 35 m of depth (Figure 5a). Given the general WSW dip of the bedding in the area, we consider the dip of these reflections as apparent due to the seismic line strike and lack of depth migration. At distance 60 m, these two reflections are interrupted and displaced at depths of 15–20 m (Figure 5a). This offset is interpreted as due to a NE-dipping normal fault. The projection at the surface of the interpreted fault (red line in Figure 5a) intercepts the topography at distance between 45 and 60 m. However, the seismic line has a low reflectivity within the first ∼10 m depth interval, insufficient to provide more details and insights on the stratigraphy and potential fault offsets. Another reflection discontinuity is visible between the distances 104–116 m (Figure 5a), although the poorly coherent reflections, and the lack of displacement, do not constrain a reliable fault image.

The GPR profile images the near surface portion of the transect, and it is characterized by continuous shallow reflections in the first two m. At depth down to 3 m, the strong attenuation caused by the moderate to high conductivity of the deposits (ERT data available on the area show resistivity generally <50 Ωm in the shallow subsurface) does not allow to clearly interpret the stratigraphy. Analyzing more carefully the geometry of the shallower reflections, these show SW-dipping reflections at distances 0–5 and 16–18 m, which could represent the conglomerates mapped in the footwall. A clear subvertical (E-dipping) discontinuity of GPR signal at ∼42 m along the profile, could be compatible with a fault, being a GPR signature including reflection truncation, dip change and diffraction hyperbola (e.g., Ercoli et al., 2013, 2021b). This GPR signature appears as the surface projection of the fault zone seen on the seismic line (Figure 5a). This GPR discontinuity was thus inferred as a possible fault zone, and it was later confirmed by ground trenching. Notice that the GPR attributes displayed in Figures 5c and 5d offer a higher degree of detail in comparison to the conventional GPR profile of Figure 5b. This consideration is confirmed not only by the enhancement of the phase discontinuity across the fault (red dashed line), but also by the emphasized gentle inflection of the shallower (hanging wall) deposits close to the fault, possibly including colluvial wedges (red arrow). In addition, the stratigraphic mapping of the deposits geometry is also strongly improved not only along the entire GPR profile, but also down to 3 m depth, where the attenuation, possibly due to conductive clayey layers, reduced the reflections amplitude in Figure 5b. This fact is particularly visible within the basal contact between the gently W-dipping reflections (black arrows in Figure 5d) and the overlying layers. The latter profile demonstrates the capability of GPR attributes to recover information which are hardly visible in conventional GPR profiles, increasing the data interpretability also in relatively unfavorable conditions caused by conductive materials.

4.2.2. Stratigraphy and Primary Tectonic Features

The Villa Sterpeto paleoseismological trench was dug to disclose the fault zone imaged by the geophysical investigations (Figure 6). The trench walls exposed 11 depositional units. The oldest continental unit, formed by gravels of the Citerna synthem (unit 11), is juxtaposed by faulting to the younger sedimentary sequence of

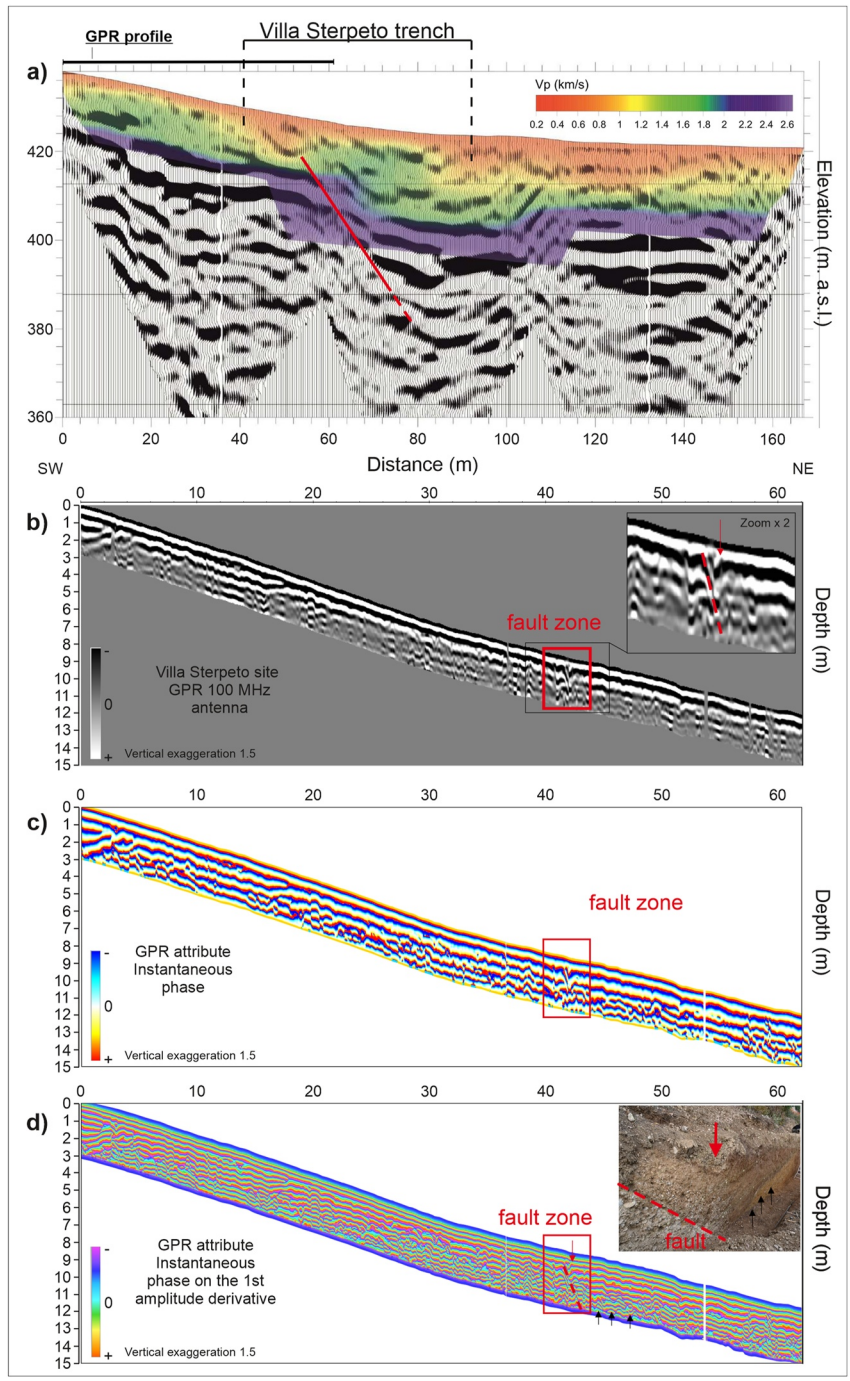

Figure 5. Geophysical data interpretation at the Villa Sterpeto site. (a) Seismic reflection profile overlapped by refraction tomography model (details in Text S1 in Supporting Information S1), and by the interpreted normal fault (red line); (b) Ground Penetrating Radar (GPR) profile; the red box points out the lateral radar discontinuity interpreted as a possible fault zone. (c) Instantaneous phase attribute enhancing the continuity of reflections as well as the fault zone; (d) the GPR attributes enhances the geometries of the subsurface stratigraphy also in deeper sectors (3 m depth) characterized by low GPR reflection amplitudes caused by high-attenuation, as well as across the fault zone; the GPR attributes aid the interpretation due to higher level of details in comparison to panel (b).

the Anghiari sub-synthem (units 7, 8, 9, and 10), colluvium containing paleosols (unit 2, 3, 4, 5, and 6) and anthropogenic deposits (unit 1). The detailed description of the stratigraphy is reported in Text S3 in Supporting Information S1.

Figure 6. Interpreted orthophotomosaic of the north-west wall of the Villa Sterpeto trench. The white squares correspond to the location of the pictures in Figure 8. The stereoplot, from left to right, represents respectively: results of anisotropy of magnetic susceptibility analysis (square, triangle, and circle are maximum, intermediate, and minimum susceptibility axes, respectively); bedding attitude; and fractures attitude. The rose diagram shows the fracture attitude measured on the trench wall (in orange) and bench (in black).

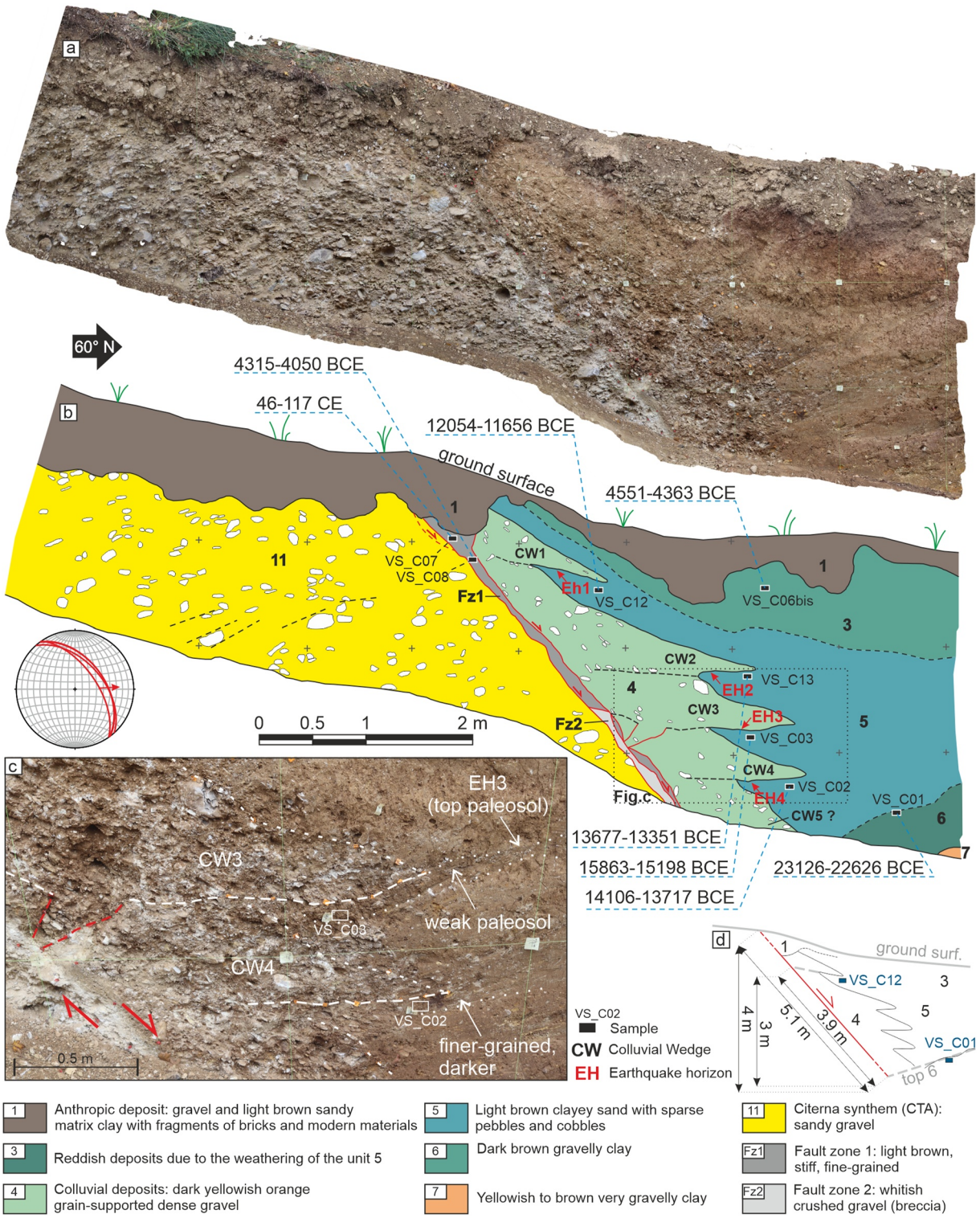

Figure 7. (a) Detailed view of the fault zone of the Villa Sterpeto trench; (b) interpretation of the fault zone of the Villa Sterpeto trench, with the age of the samples; (c) detail of the colluvial wedges CW3 and CW4 and the corresponding earthquake horizons; (d) simplified scheme of displacement measure to compute the slip rate; The attitude of the fault and the corresponding slip vector are shown in the stereo plot.

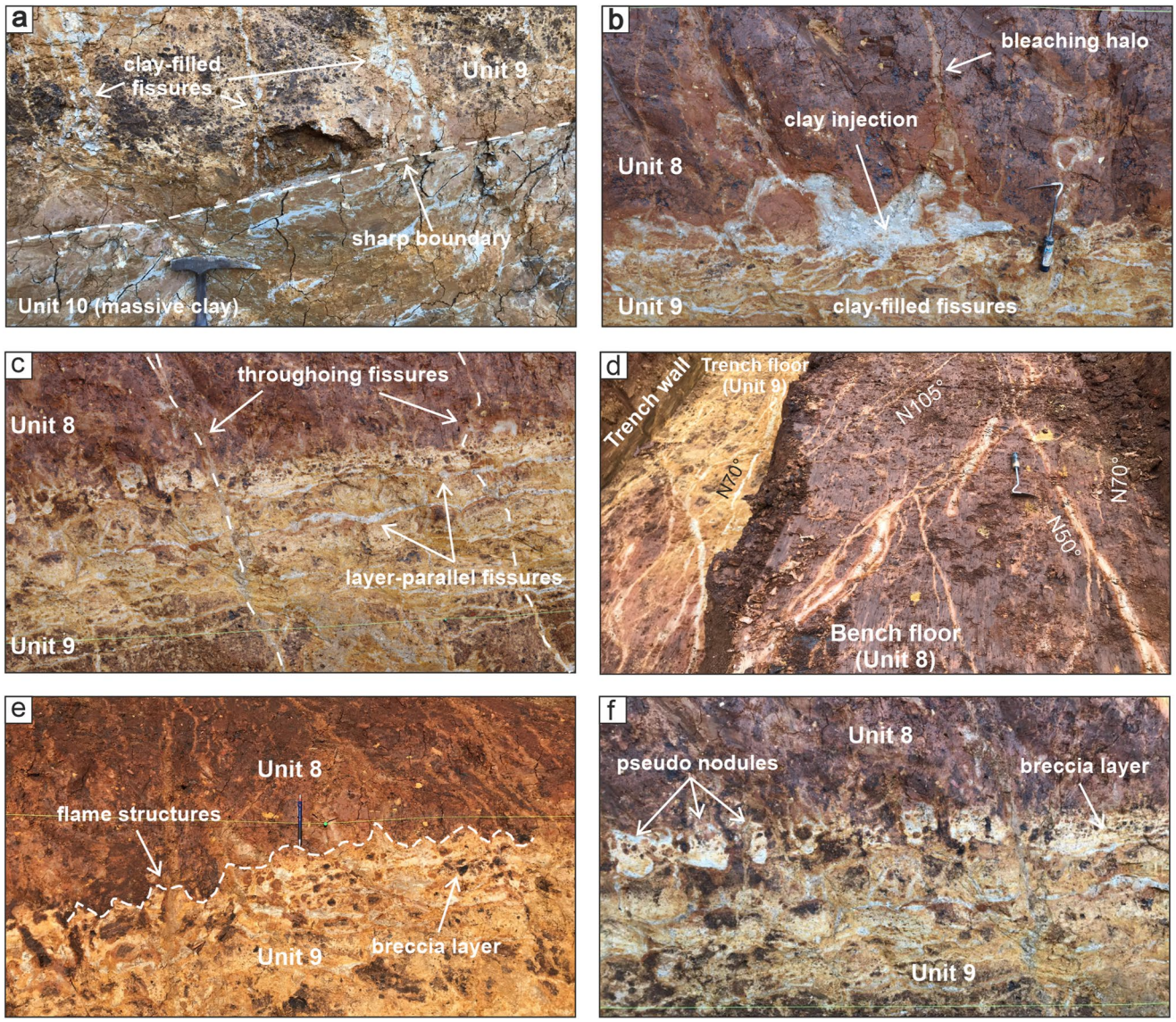

Figure 8. Detailed views of soft-sediment deformation within units 8 and 9. Clay injections and clay-filled fissures are sourced by unit 10. Location in Figure 6. Panel (d) is an oblique view to NNE of the trench and bench floors.

The fault affects the entire trench wall up to the base of the topmost unit (unit 1), with a sharp contact, 10-20 cm-wide thickening in the upper part, dipping 50° toward NE (Figure 7). In particular, the fault mean attitude is 052/52 (dip direction/dip) with variable value of dip ranging from 48° to 60°; the slip vector measured on striae trends 85°N and the plunge is 57°. Based on its lithological and chromatic features, the fault zone is divided into a stiff light brown fine-grained, organic rich fault zone (FZ1) and a whitish fault zone made of crushed gravel, outcropping in the lower part of the trench (FZ2). Locally, FZ1 and FZ2 are separated by a shear surface. Two samples of FZ1 bulk sediments were collected for radiocarbon dating (VS_C07 and VS_C08), providing ages of 46–117 CE and 4,315–4,050 BCE, respectively (Table 1).

In the hanging wall of the fault, the colluvial unit 4 forms four coarse-grained wedge-shaped bodies of material colluviated from unit 11 that interfinger with unit 5 (CW1-4 in Figure 7). An additional wedge-shaped fifth body (CW5?) is partially visible in the lowest part of the trench wall. The four wedge-shaped bodies are stacked with similar shape and size. Their geometric settings, suggests an accumulation controlled by episodes of footwall exhumation. A mechanism able to explain all those features is the rapid formation of a scarp due to surface faulting events, and consequent accumulation of scarp-derived colluvial wedges in proximity of the fault due to scarp degradation (colluvial wedge model in McCalpin (2009)).

Based on the gravel fabric, it is possible to estimate a maximum wedge thickness of 45 cm with large uncertainty. The thickness of the wedge CW5 is uncertain since it is partially buried.

CW4 and CW3 have comparable lateral extension and their tip is lying on darker and fine-grained horizons. Particularly, CW3 overlays a 5 to 10 cm-thick weak paleosol, which possibly corresponds to the topographic surface immediately before the onset of coarse-grained colluvial sedimentation (Figure 7c). Between CW3 and CW4 an open fissure branches from the main fault zone and is infilled with the same material of the wedge. CW2 is steeper and thicker near the fault, with a few cm-thick fine-grained layer, possibly corresponding to a weak soil horizon, at the base of its tip. CW 1 is the smallest wedge and does not show a clear fine-grained horizon at its base. All the wedges are faulted. In order to constrain the age of each wedge formation, and thus of related episodes of footwall exhumation, we collected samples for radiocarbon dating of the fine-grained organic layers of unit 5, at their bases, paying attention to collecting the most organic layers. Due to the lack of charcoals in all of the units, the dating was performed on the bulk organic fraction contained in the sediments. Moreover, we sampled the units 6 and 3 which are the lowermost and uppermost boundaries of the entire colluvial unit, respectively. The hanging wall depositional sequence from unit 6 to 10 is tilted against the fault. The mean layer attitude in the trench is 265/12 (dip direction/dip). The dip of the boundary between units 6 and 7 becomes progressively steeper toward the fault, from 5° to 25°, suggesting syn-depositional back-tilting. In the nearby of the trench, in the hanging wall of the fault, the Citerna synthem is tilted up to 35° toward the west. This geometrical setting can be interpreted as large-scale, fault-related hanging wall back-tilting that created accommodation space for the deposition of units 1 to 5. To measure the displacement of the fault we used the buried paleosol of unit 6, the top of which should correspond to an ancient topographic surface. The top of unit 6 is displaced about 4 m vertically (5.1 m along-dip slip) with respect to the nowadays topographic surface. Since the topographic surface may have been reshaped, this should correspond to the minimum fault displacement accumulated since the age of unit 6 (23,126–22,626 BCE, sample VS_C01) (Table 1).

4.2.3. Fissures and Other Secondary Features

Many fractures, fissures and other soft-sediment deformation affect units 9 and 8 (Figure 6). A sharp boundary separates unit 9 from the underlying massive gray clays of unit 10 (Figure 8a). In general, the fissures have an aperture in the order of 0.5–2 cm and are infilled with clay material from unit 10. Other fractures, without measurable aperture, are highlighted by a cm-sized bleaching halo, particularly evident in the red-colored unit 8. Unit 9 is pervaded by both layer-parallel and layer-perpendicular (or oblique) fissures (Figure 8b). Most of them are confined within unit 9, while some of them cut through both units 9 and 8 perpendicularly to the bedding (Figure 8c). Layer-perpendicular fractures with bleaching halo prevail in unit 8. When observed on the SE-facing wall of the trench, the layer-perpendicular fissures, and fractures dip apparently to the NE, as they are tilted with the hosting sedimentary beds (Figure 6). Nevertheless, the true dip is nearly vertical; the measured strikes cluster around values of 70° ± 10° (stereonet in Figure 6). In map view (on the bench floor, Figure 8d), some fractures form approximately conjugate systems, with acute angles of 45°–60°. Overall, the strikes measured on the trench wall and on the bench floor are dispersed between 30° and 120°, with a main cluster at 70° ± 10° (the bisector of the acute angle) and two secondary clusters at 105° ± 5° and 50° ± 15° (rose diagrams in Figure 6).

The boundary between units 8 and 9 is affected by soft-sediment deformation of different types. At places, flames of clay injections fed by fissures from unit 9 intrude into the bottom part of unit 8, forming "jester hat-like features" (Figure 8b). Often, the stratigraphic transition is characterized by a 10–15 cm-thick breccia layer formed by angular clasts from unit 8 in the matrix of unit 9, which indicates mixing along the boundary between the two units. The breccia layer can intrude slightly into the overlying unit 8, forming flame structures (Figure 8e), or can be coated by clay material, forming pseudo-nodules (Figure 8f). The interpretation of these features as due to earthquake-induced ground shaking would give insights on the recurrence of strong earthquakes on the Sansepolcro basin fault system, as argued in the discussion section.

4.2.4. Anisotropy of Magnetic Susceptibility

The results of the AMS analyses are reported in Figure S5 and Table S1 in Supporting Information S1. The mean susceptibility on the sites collected in the clays varies from 139 to 217 e−6 SI, while the sites collected in the paleosol and in the colluvial unit containing the wedges have higher susceptibility, from 888 to 7,162 e−6 SI. All sites are characterized by a well-defined AMS tensor. The shape of the ellipsoids, T, varies from weakly oblate (ANGH01, 02, 04, 05) to strongly prolate (ANGH03) and one site is triaxial (ANGH08). The degree of

anisotropy, P_j, indicates that the sites vary from weakly anisotropic (4% of ANGH01) to strongly anisotropic (43%, ANGH08), approaching the fault trace. The orientation of the k_{max} axis, that can represent the direction of the magnetic lineation (k_{max}/k_{int}), is mostly shallowly oriented NE-SW, and it is orthogonal to the foliation plane (k_{int}/k_{min}), oriented NW-SE, steeply dipping to the NE. The anisotropy data suggest that a primary sedimentary fabric has been overprinted by an incipient to intense tectonic fabric as confirmed by the evolving AMS tensor shape from purely oblate farther from the fault to oblate and prolate approaching the fault.

The magnetic foliation orientation is mostly NW-SE, thus sub-parallel to the fault plane. The magnetic lineation is orthogonal to the ATF and parallel to the NE–SW-oriented direction of extension revealed by both regional active stress field (Montone & Mariucci, 2016) and Quaternary strain indicators (Lavecchia et al., 2022). These results are comparable with the stretching direction inferred by Maffione et al. (2012) through the AMS analysis of the Lower Pleistocene Fighille synthem at a nearby site, south of the Anghiari ridge (their site SANS).

In summary, the AMS indicates continuous extension across the stratigraphy exposed in the trench. When compared with data from the literature, our results suggest that in the study area an extensional stress field has been continuously active since the Early Pleistocene.

4.3. Todari Site

The Todari roadcut was dug across a secondary strand of the Micciano section. The outcrop exposes 7 units, a NE-dipping main normal fault zone and a sub-vertical antithetic splay (Figure 9). The main fault juxtaposes an Early Middle Pleistocene unit, part of the Citerna synthem, from a Holocene succession formed by, from the bottom to the top, a paleosol (unit 6), clayey palustrine deposits (unit 5), clayey-sandy colluvial units (unit 2 to 4) and the present-day soil (unit 1). An additional unit is the infill of a fissure topped by unit 4 (FF, filled fissure). The detailed description of the stratigraphy is reported in Text S3 in Supporting Information S1.

4.3.1. Primary Tectonics Features

The Todari roadcut is characterized by several synthetic normal fault splays dipping 40°–50° toward NE. The main fault zone (FZ in Figure 9) is composed of fault brecciated sand coming from the faulting of unit 7. The hanging wall of the main fault zone includes two synthetic splay dipping from 60° to 80° toward NE and connected to the principal fault in the upper part. Another synthetic splay displaces the boundary between units 6 and 7 in the hanging wall of the main fault. This fault dips 50° at the bottom of the trench and becomes progressively steeper upwards, up to overturn close to the surface. Unit 4, 5, and 6 are faulted and dragged against the main fault zone, whereas units 3 and 2 are deposited after the last apparent deformation episode. A sub-vertical antithetic splay, located in the hanging wall at ~2 m from the main fault, displaces by 20 cm the boundary between units 6 and 7.

4.4. Anghiari Sites A and B

The site A trench was excavated across the trace of the Anghiari-Motina fault section, while the site B trench was excavated in the hanging wall of the fault. The site B trench cut across the MTC synthem and provided constraints on the stratigraphy of the hanging wall, which helped us in constraining the displacement accumulated after the deposition of the MTC (Figure 3). The orthophotomosaic of the site B trench and its stratigraphic description are provided as Figure S4 in Supporting Information S1. In the following, we describe the site A trench, which is characterized by 12 depositional units and 3 high-angle tectonic contacts (Figure 10). The main tectonic contact downthrows to the NE the stratigraphic succession older than unit 2. The youngest unit (unit 1) is an anthropogenic backfill. Units 2 to 8 are colluvial deposits, the youngest of which (unit 2) is historical (contains pottery shards). Unit 9 is a remnant of an alluvial terrace. Unit 10 is made of gravel and sand belonging to the CTA synthem. The clayey unit 11 is the oldest unit, possibly belonging to the Fighille synthem. The detailed description of the stratigraphy is reported in Text S3 in Supporting Information S1.

4.4.1. Primary Tectonics Features (Site A)

The site A trench wall exposes three barely visible fault zones (FZ1, 2 and 3 in Figure 10). Between FZ1 and FZ3 the depositional sequence and the faults are cut by a gravitational sliding surface (green line in Figure 10) with slip direction to the NE (i.e., downslope). The gravitational sliding postdates the faults and is covered by unit 2 (containing reworked pottery shards of VII-XIV century CE).

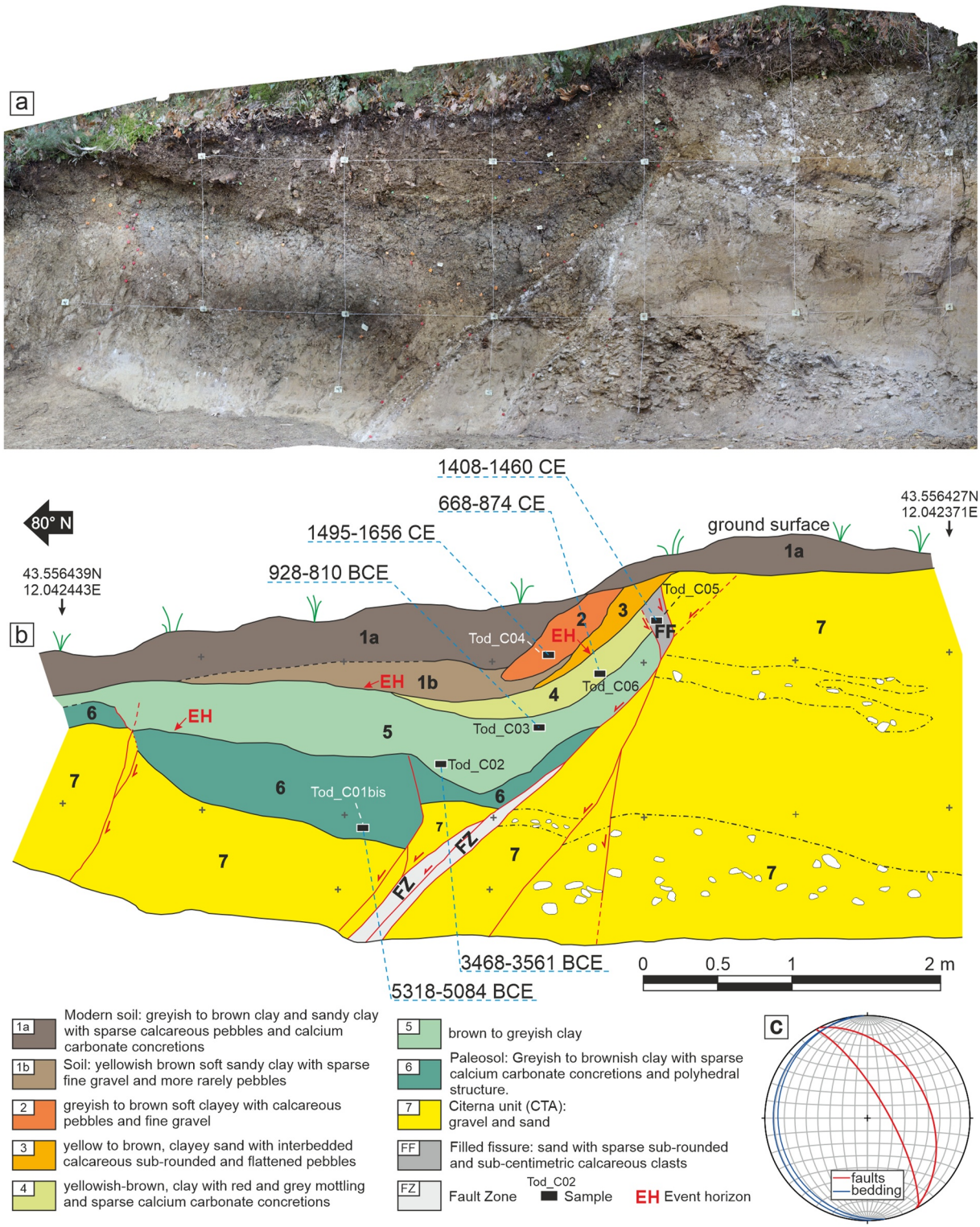

Figure 9. (a) Detailed view of the Todari roadcut; (b) interpretation of the Todari roadcut, with the age of the samples; (c) the attitude of the fault and bedding are shown in the stereo plot.

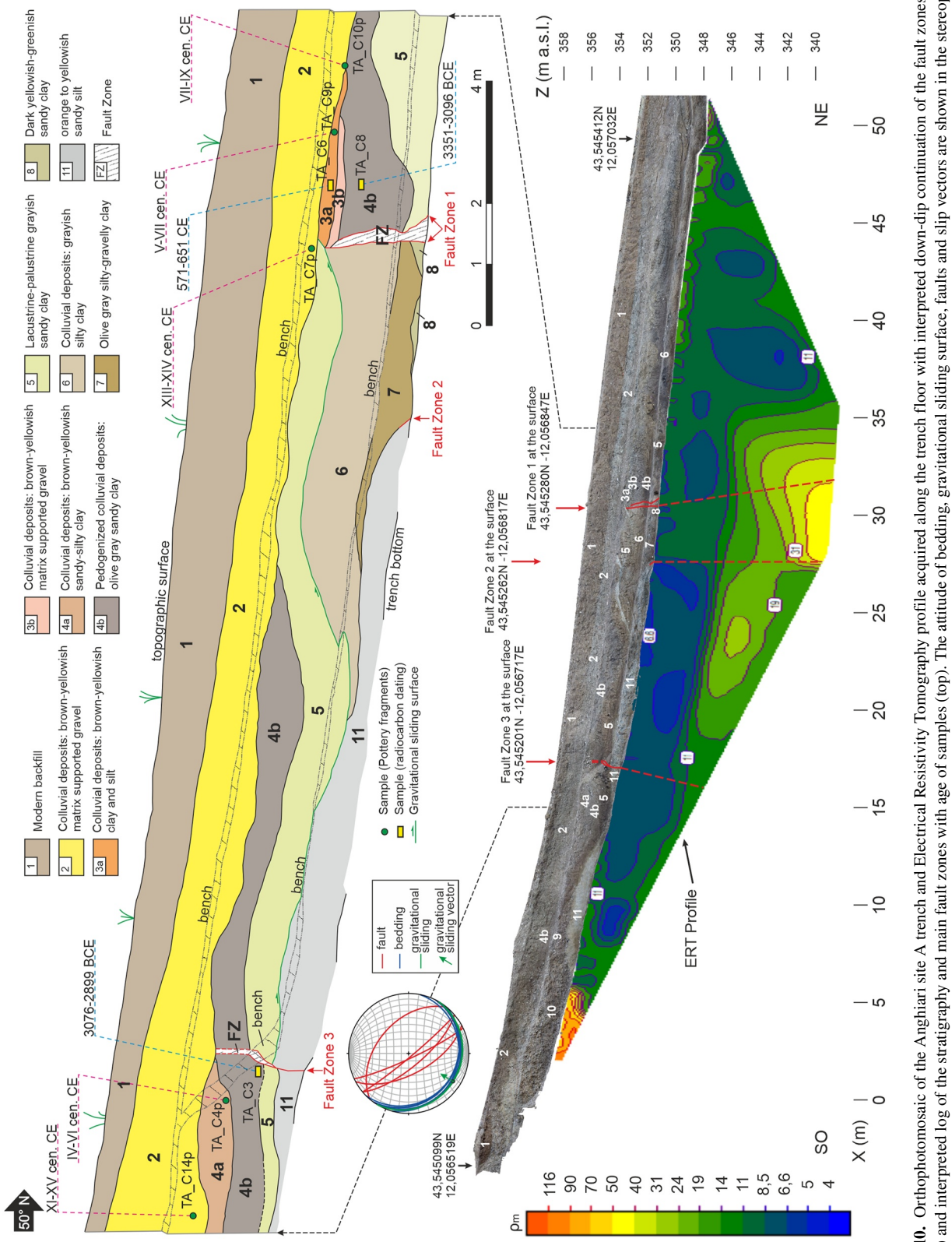

Figure 10. Orthophotomosaic of the Anghiari site A trench and Electrical Resistivity Tomography profile acquired along the trench floor with interpreted down-dip continuation of the fault zones (bottom) and interpreted log of the stratigraphy and main fault zones with age of samples (top). The attitude of bedding, gravitational sliding surface, faults and slip vectors are shown in the stereoplot.

The main fault zone (FZ1, Figure 10) is formed by two nearly parallel high-angle fault strands downthrowing by a minimum of 1.75 m to the NE the contact between units 4b and 5. In the hanging wall of the main fault there are two colluvial units (3a and 3b). Unit 3b is wedge-shaped and thickens close to the fault, suggesting that its sedimentation can be related to the fault. It is not clear if unit 3b is faulted or simply rests on the fault surface. The geometry of unit 3a is undetermined, as its western edge is cut by the gravitational sliding surface and its upper part is truncated by unit 2. The possible meaning of units 3a and 3b in relation to the fault activity will be discussed in the next section. The fault zone is sealed by the gravitational sliding surface and by unit 2, which has an age not older than VII-XIV centuries CE, or younger, on the basis of the findings of reworked pottery shards.

A sharp, high-angle lateral contact between unit 7 and unit 11 (FZ2, Figure 10), located 3 m upslope FZ1, can be interpreted as a tectonic contact sealed by the upper part of unit 7.

The third fault zone (FZ3, Figure 10), formed by two antithetic strands downthrowing by ~10 cm to the SW the base of unit 4b, is sealed by unit 2. In order to constrain the fault prosecution at depth, we acquired an ERT along the trench floor. The ERT profile reported in Figure 10 was obtained by the joint inversion of the Wenner and dipole-dipole acquisitions. The contact between the gravels of the Citerna synthem and the underlying clays and silts is evident in the first meters of the profile. A sharp lateral resistivity variation, from <40 to 40–50 **Ω**m is present in the center of the profile and corresponds to the down-dip continuation of FZ2. The down-dip continuation of FZ1 is not particularly evident but can be the cause of the eastward lateral transition to lower resistivity values from 40–50 to <15 **Ω**m. There is no evidence in the profile of FZ3, probably because the limited displacement does not produce a lateral resistivity variation.

5. Discussion

5.1. Paleoearthquakes

At the Villa Sterpeto site the presence of five stacked colluvial wedges (CW in Figure 7) against the fault suggests the occurrence of as many discrete and recurrent surface faulting earthquakes. Each earthquake is thought to have produced a coseismic fault scarp at the surface (free face). The erosion of the exhumed scarp would have caused the deposition of colluvial material in the hanging wall of the free face, on top of the downthrown ground surface. This hypothesis is supported by the presence of fine-grained, moderately organic layers below the wedges, particularly developed beneath CW3 (i.e., the weak paleosol at the base of CW3, see Figure 7c). Those fine-grained organic layers can be interpreted as the earthquake horizons (hereinafter EH), that is, the topographic surface at the time of the surface faulting earthquakes. Moreover, the termination of the open fissure located below CW3, possibly corresponds to the boundary between CW3 and CW4, that is, the earthquake horizon EH3 (see Figure 7). In addition, a fault activity during the colluvial accumulation is required to explain the formation of the space necessary for the stacking of the wedges in the hanging wall of the fault and their later faulting. Based on the above considerations, we interpreted the colluvial wedges as tectonic in origin.

Thanks to the radiocarbon dating, we constrain the age of each EH and therefore hopefully the closest *pre faulting* age of each earthquake. The reconstructed chronology of the surface faulting earthquakes is reported in Figure 11 and in Table 2.

CW1 was deposited immediately after 12,054–11,656 BCE (sample VS_C12, collected below the wedge), and before 4,551–4,363 BCE (sample VS_C06bis, collected within unit 3). Therefore, the age window for E1VS is between 12,054 and 4,363 BCE. CW2 was deposited immediately after 13,677–13,351 BCE (sample VS_C13, collected below the wedge), and before 12,054–11,656 BCE (sample VS_C12, collected above the wedge). Therefore, the age windows for E2VS is between 13,677 and 11,656 BCE. Because of the out of sequence ages of the samples VS_C03 and VS_C02 we advanced two different hypotheses concerning the age of the events E3VS and E4VS:

1. Hypothesis 1 excludes sample VS_C03 due to significant age inheritance, beyond the calibrated age uncertainty, caused by contamination from old material reworking. CW3 and CW4 would have deposited both between 14,106–13,1717 and 13,677–13,351 BCE (samples VS_C02 and VS_C13). Therefore, E3VS and E4VS both occurred between 14,106 and 13,351 BCE.
2. Hypothesis 2 excludes sample VS_C02, thus assuming contamination by young carbon that provides an age younger than the overlying sediments. CW3 would have deposited immediately after 15,863–15,198 (sample VS_C03) and before 13,677–13,351 BCE (sample VS_C13). CW4 would have deposited after 23,126–22,626 BCE (sample VS_C01) and before 15,863–15,198 (sample VS_C03) (Figure 7). Therefore,

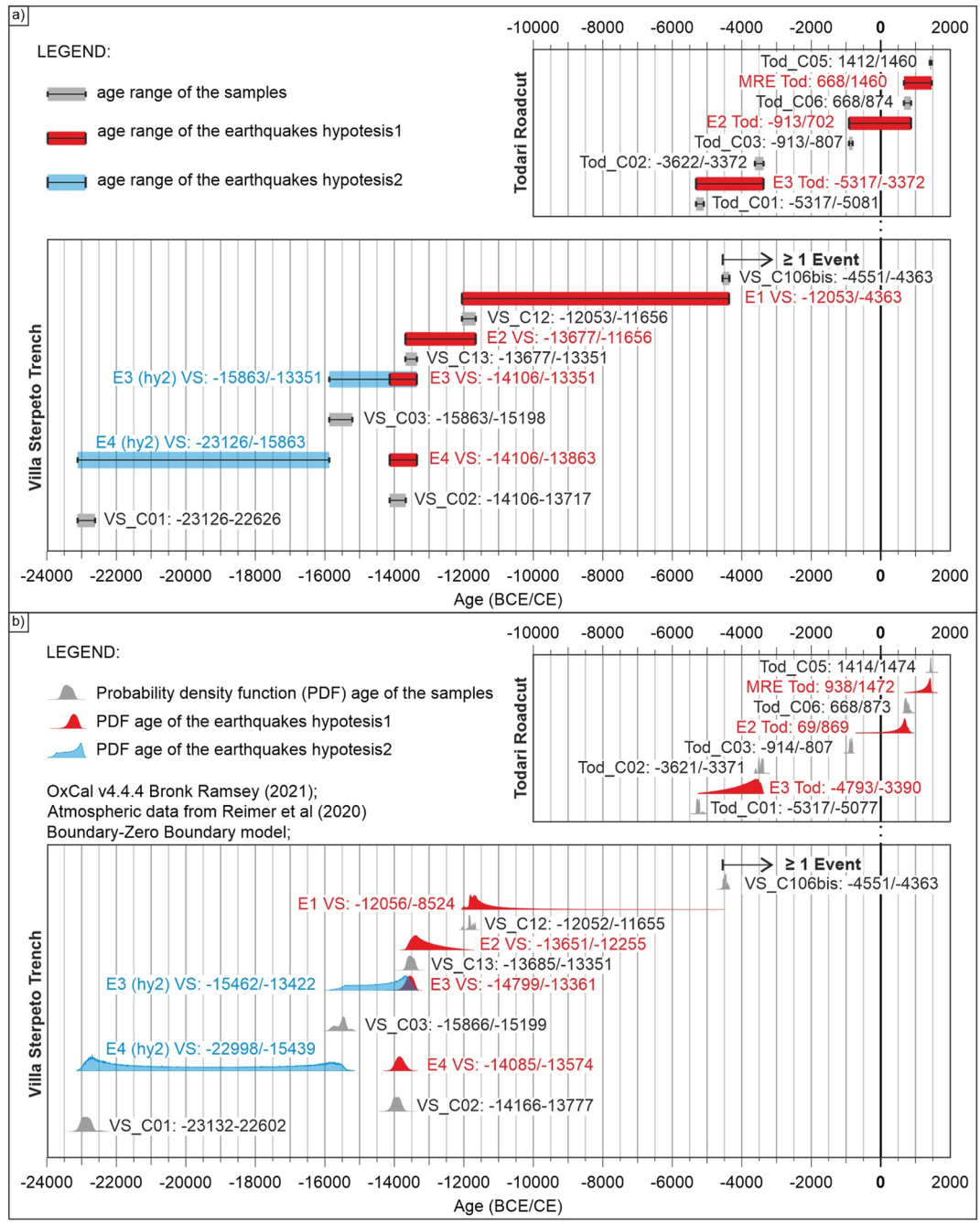

Figure 11. (a) Summary of the seismic history of the Anghiari fault showing the age windows of each earthquake corresponding to the time window between the age of a couple of samples. Referring to E4_VS and E3_VS the hypothesis 2 is represented in blue. (b) Summary of the seismic history of the Anghiari fault showing the probability density function related to the age of each sample and each earthquake, computed using the Boundary-Zero Boundary approach in OxCal. Referring to E4_VS and E3_VS the hypothesis 2 is represented in blue.

E3VS occurred between 15,863 and 13,351 BCE, while E4VS occurred between 23,126 and 15,863 BCE. Since the base of the wedge 5 and its chronological relationship with unit 6 (sample VS_C01, 23,126–22,626 BCE) are buried below the trench floor, it is not possible to exclude that, in the time interval relative to E4VS (23,126–15,863 BCE), more than one earthquake has occurred.

Hypothesis 1 involves a cluster of earthquakes in a short time window, while hypothesis 2 provides a more regular slip history. Hypothesis 1 implies the discard of a sample (VS_C03) contaminated by old carbon, which

Tectonics

10.1029/2023TC007798

Table 2
Summary of the Paleoearthquakes Ages and Features

Trench	Fault	Coord. of the fault at surface		Fault attitude (imm./ incl.)	Event *n.*	Evidence	Maximum age			Minimum age			Preferred age (OxCal Byesian model)	Maximum vertical thickness (hCW, m)	Displacement (*D*, m)	Type D
		Longitude	Latitude				Max	Min	Sample	Max	Min	Sample				
Todari Roadcut	Micciano Sec	12.0423	43.5563	058/40	MRE Tod	FF—D	874 CE	668 CE	Tod_C06	1,460 CE	1,408 CE	Tod_C05	938–1,472 CE	0.25	0.35	FF; D
Todari Roadcut	Micciano	12.0423	43.5563	058/40	E2 Tod	D	928 BCE	810 BCE	Tod_C03	874 CE	668 CE	Tod_C06	69 CE–869 BCE	0.3	0.52	D
Todari Roadcut	Micciano	12.0423	43.5563	058/40	E3 Tod	S	5,318 BCE	5,084 BCE	Tod_C01bis	3,561 BCE	3,468 BCE	Tod_C02	4793–3,390 BCE	/	0.18	V
Villa Sterpeto	Micciano	12.0457	43.552	052/51	E1 VS	CW	12,054 BCE	11,656 BCE	VS_C12	4,551 BCE	4,363 BCE	VS_C06 bis	12,056–8,524 BCE	0.45	/	CW
Villa Sterpeto	Micciano	12.0457	43.552	052/51	E2 VS	CW	13,677 BCE	13,351 BCE	VS_C13	1,2054 BCE	11,655 BCE	VS_C12	13,651–12,255 BCE	/	/	CW
Hypothesis1 (No sample C03)																
Villa Sterpeto	Micciano	12.0457	43.552	052/51	E3 VS	CW	14,106 BCE	13,717 BCE	VS_C02	1,3677 BCE	13,351 BCE	VS_C13	14,799–13,361 BCE	0.45	/	CW
Villa Sterpeto	Micciano	12.0457	43.552	052/51	E4 VS	CW	14,106 BCE	13,717 BCE	VS_C02	13,677 BCE	13,351 BCE	VS_C13	14,085–13,574 BCE	0.45	/	CW
Hypothesis2 (No sample C02)																
Villa Sterpeto	Micciano	12.0457	43.552	052/51	E3 VS	CW	15,863 BCE	15,198 BCE	VS_C03	13,677 BCE	13,351 BCE	VS_C13	15,462–13,422 BCE	0.45	/	CW
Villa Sterpeto	Micciano	12.0457	43.552	052/51	E4 VS	CW	23,126 BCE	22,503 BCE	VS_C01	15,863 BCE	15,198 BCE	VS_C03	22,998–15,439 BCE	0.45	/	CW

Note. MRE = Most Recent Earthquakes, V = Vertical displacement, S = Dislocation of stratigraphic horizon, CW = Colluvial Wedge, *D* = Dragging, and FF = Filled Fissure.

has been demonstrated to be likely due to reworked organic detritus or age inheritance (Rockwell et al., 2022). Nevertheless, sample VS_C03 was collected in one of the most evident buried paleosol within the colluvial unit. This makes the sample more reliable than others. On the other hand, we cannot exclude that younger carbon could have contaminated sample VS_C02. Since earthquake clustering is quite common in the Apennines (as Chlorine 36 studies suggest, e.g., Benedetti et al., 2013; Cowie et al., 2017; Mildon et al., 2022; Schlagenhauf et al., 2011), there are no particular criteria to prefer one hypothesis to the other.

Since CW1 is faulted, there is evidence of at least an earthquake younger than E1_VS. Such event(s) would be compatible with the tectonic folding of the unit 3 bottom (4,551–4,363 BCE, sample VS_C06bis). According to the age of the organic material trapped and sheared within the fault zone (sample VS_C08) this earthquake could be post 4,315–4,050 BCE. At the Todari roadcut, the restoration of the tectono-stratigraphic setting allowed us to reconstruct three surface faulting events (Figure 12). The oldest event (earthquake E3 Tod) caused the displacement of the boundary between units 6 and 7 along the synthetic and antithetic splays in the hanging wall of the main fault (Figure 12b). This earthquake occurred after 5,318–5,084 BCE, age of unit 6 (sample Tod_C01bis) and before 3,468–3,561 BCE, age of unit 5 (sample Tod_C02). The net slip measured on the synthetic splay was 18 cm, with a minimum net throw of 14 cm. This can be considered as the minimum surface displacement of the earthquake because some slip could have occurred along the main fault, which shows no visible piercing points (Figure 12b). After E3 Tod, an erosional event, possibly caused by water running parallel to the fault, reshaped the top of unit 6, erasing the evidence of slip along the synthetic fault (Figure 10c). The age of E3 Tod could be comparable to the age of the earthquake faulting CW1 at the Villa Sterpeto trench. Earthquake E2 Tod occurred after 928–810 BCE, age of unit 5 (sample Tod_C03) and before 668–874 CE, age of unit 4 (sample Tod_C06) (Figure 12e). This event caused a minimum net slip along the main fault of 52 cm (minimum throw of 35 cm), including the dragging of units 5 and 6 and rotation of the high angle splay in the upper part of the main fault (Figure 12e). The subsequent erosion of the fault scarp caused the deposition of a colluvial wedge (unit 4) (Figure 12f). The most recent earthquake (MRE Tod) caused the opening of a fissure in correspondence of the rotated synthetic splay and the dragging of units 4, 5 and 6 (Figure 12g). The minimum net displacement along the main fault was 35 cm (minimum throw of 23 cm). After the MRE, because of the erosion of the scarp, the fissure was filled and another colluvial wedge was formed (unit 3) (Figure 12h). The MRE occurred after 668–874 CE, age of unit 4 (sample Tod_C06) and immediately before 1,408–1,460 CE, age of the infilling of the fissure (sample Tod_C05). The fissure infill is rich in organic matter. It is likely that the fissure was infilled by material from the soil at the time of the surface faulting. Therefore, the age of the infill should be close to the occurrence of the event. The minimum cumulative net slip of the last three earthquakes is 1.05 m (minimum cumulative throw of 0.72 m) accumulated since 5,318–5,084 BCE.

The age constraints bracketing the event windows for the Villa Sterpeto and Todari sites are summarized in Figure 11a and Table 2. Using the Boundary-Zero Boundary model, we performed a Bayesian analysis in OxCal v4.4.4 at the Villa Sterpeto site skewing the age of the earthquakes thanks to the samples collected immediately below the colluvial wedges, that is, within the earthquake horizons. At the Todari roadcut we used the same methodology to constrain the age of MRE_Tod close to the age of the infilling of the fissure (sample Tod_C05); the age of E2_Tod close to the deposition of the colluvial wedge corresponding to unit 4 (sample Tod_C06); and the age of E3_Tod close to the age of the base of unit 5. The obtained ages are reported in Figure 11b.

At the Anghiari site A the colluvial wedge 3a, possibly faulted, suggests the occurrence of one or two surface faulting earthquakes occurred between 3,351–3,096 BCE and XIV century (or shortly after, considering that the pottery shards are reworked), the ages of unit 4b and 2, which are comparable with the time windows of the youngest events of the Todari roadcut site. The youngest recognized earthquake occurred in historical time (938–1,472 CE, Figure 11b). Two historical earthquakes hit the Sansepolcro basin in that time interval or close to it, the 1458 and 1489 earthquakes (Figure 2), with the 1458 being the strongest (epicentral intensity VIII-IX, Mw 5.8). Therefore, the youngest surface faulting event might correspond to one of these two earthquakes, possibly the 1458 event, which fit the time window of the surface faulting event. Unfortunately, the 1458 event is poorly constrained by macroseismic data. The Anghiari town, the nearest town to the studied fault, has no macroseismic information on both the 1458 and 1489 events. The 1458 earthquake produced damages of intensity VIII-IX in both Città di Castello, in the southern edge of the basin, and in Sansepolcro, 15 km north of Città di Castello and only 7.5 km east of Anghiari. Damage of intensity VII-VIII was documented for a locality sited 13 km south of Città di Castello. In this context, it seems unlikely that the earthquake did not damage Anghiari, at a distance of 17 km to Città di Castello

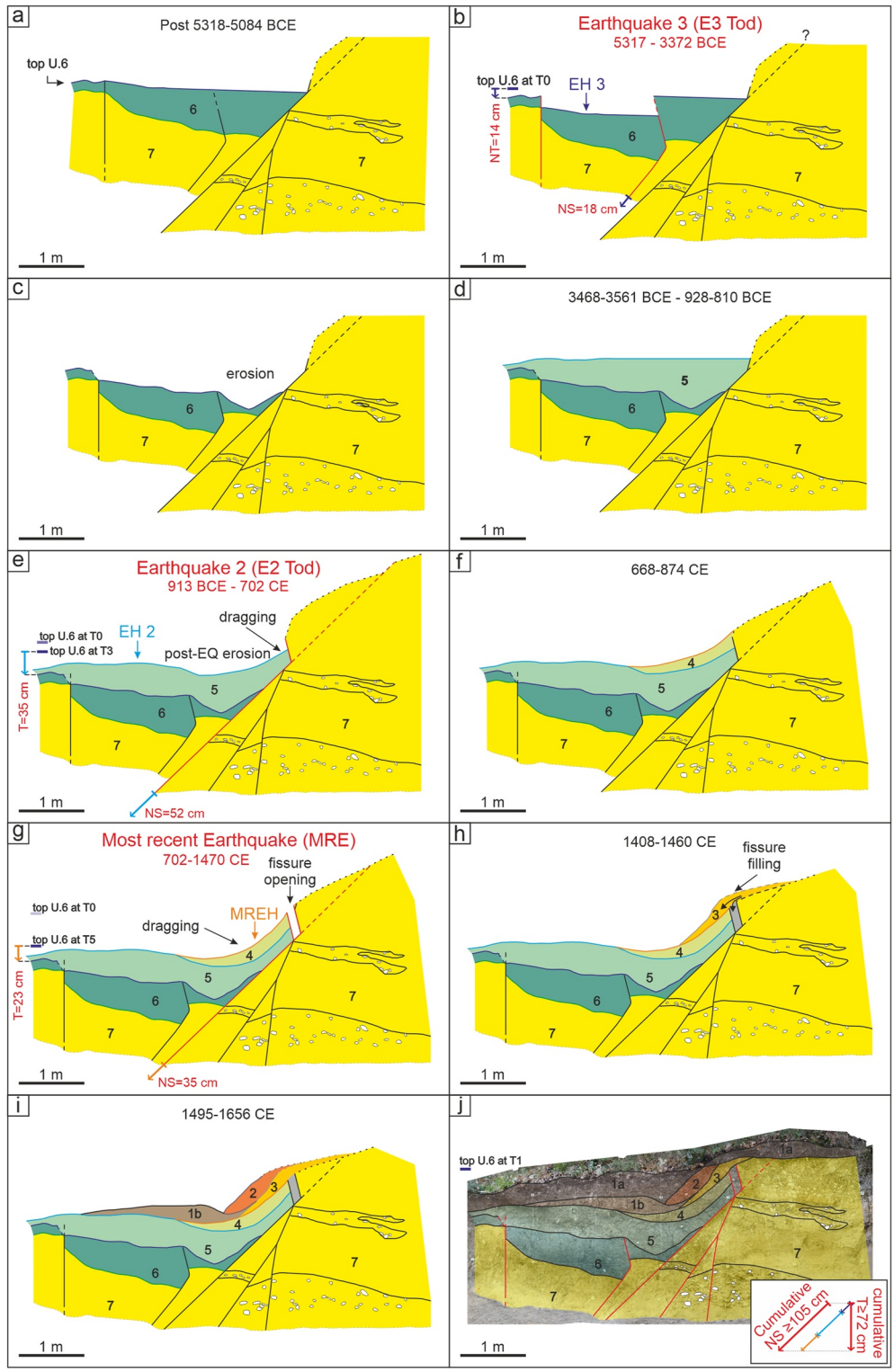

EH = earthquake horizon (ground surface at the time of earthquake surface faulting);T = throw NT = net throw; NS = net slip

Figure 12.

and 7.5 km to Sansepolcro, within the same sedimentary basin. The lack of macroseismic information in Anghiari is possibly due to a gap in the historical documentation. Therefore, we suggest that the 1458 earthquake was caused by reactivation of the Anghiari fault, and possibly of the entire Anghiari-Città di Castello main fault. In summary, combining the data from all the paleoseismological investigations, we recognized

Table 3
Recurrence Time Interval and Coefficient of Variation Computed Using the RP Tool of the FISH Tools Package (Pace et al., 2016) for Both the Earthquakes Ages Hypothesis and Using Only the Age of the Samples or the Ages Obtained Using OxCal

Paleoearthquakes age constraints	Paleoearthquakes age hypothesis	Recurrence interval (years)	Coefficient of variation
Age of the samples	1	2,495	0.94
Age of the samples	2	3,104	0.65
OxCal	1	2,562	0.92
OxCal	2	3,230	0.62

nine different earthquakes in the last 22 ka and an additional one possibly older than 25 ka. The most recent event possibly corresponds to the 1458 historical earthquake. These events broke the surface along the Micciano section of the Anghiari fault (Villa Sterpeto site), the secondary splay located in its footwall (Todari roadcut) and, at least the two most recent earthquakes also could have broken the Anghiari-Motina section (Anghiari site A). These sites might show two different parts of the same seismic history: (a) the oldest part (22,000 to 4,500 BCE) at the Villa Sterpeto site; (b) the youngest part (5,200 BCE to 1,437 CE) at the Todari roadcut and Anghiari site A sites.

5.2. Recurrence Intervals and Coefficient of Variation

The mean recurrence time interval has been estimated from our paleoseimological earthquake time series and its uncertainties in dating, with a Monte Carlo simulation approach through the tool RP included in the FISH tools package for seismic hazard assessment (Pace et al., 2016, code available at http://fault2sha.net/wp-content/uploads/2020/07/FiSHvers1.02.zip). Given the time windows of a series of paleo-events the RP tool produces a number of earthquake catalog simulations and computes the average recurrence time and its coefficient of variation (CV), namely the standard deviation of the recurrence times over their mean. CV is a critical parameter for time-dependent seismic hazard estimates, it is often poorly constrained (e.g., Ellsworth et al., 1999; Visini & Pace, 2014), and small differences in the values can lead to large differences in earthquake probability evaluation. In Table 3 are reported the computed values of mean recurrence time intervals based on the constrained age of the paleoearthquakes for both the earthquake ages hypotheses and considering both the time windows between each couple of samples (see Figure 11a) and the earthquakes age obtained using OxCal v4.4.4 (see Figure 11b). Considering that, in hypothesis 2 (quasi-periodic slip history), within the time windows related to the event E4_VS more than one earthquake may have occurred, this event has been excluded from the computation. While, for hypothesis 1 (clustering) all the events have been considered. Using only the age of the samples as constraints for the age of the earthquakes, the mean recurrence time interval ranges between 2,495 and 3,104 years, with a CV of 0.94–0.65 (for hypothesis 1 and hypothesis 2 respectively). Using the earthquake time windows from the Bayesian model computed in OxCal, the mean recurrence time interval ranges between 2,562 and 3,230 years with a CV of 0.92–0.62 (for hypothesis 1 and hypothesis 2 respectively). Both the Recurrence time interval and the CV are affected by the choice of the hypothesis, while they are not affected by the ages used as input in the computations (age of the samples rather than OxCal). In general: (a) for hypothesis 1 the recurrence time interval is shorter, but the CV is higher, indicating a non-periodic behavior. (b) for hypothesis 2 the recurrence time interval is higher, but the CV is lower, indicating a more periodic behavior.

5.3. Slip Rates

The minimum fault displacement measured at the Villa Sterpeto site (5.1 m accumulated since the age of unit 6, i.e., after 23,126–22,626 BCE) provides an average post-25 ka BP slip rate of 0.2 mm/yr. This slip rate is apparent, as it includes both closed and open seismic cycles. In order to consider only closed seismic cycles, the displacement of the top of unit 6 can be measured compared to the topographic surface immediately before the sedimentation of wedge CW1. In this case the displacement is about 3.9 m in a time window between 23,126–22,626 and 12,054–11,656 BCE (Figure 7b). This corresponds to a slip rate of 0.29–0.31 mm/yr.

Figure 12. Restoration of the Todari roadcut starting from the pre E3_Tod to the nowadays configuration. (a) Pre E3_Tod and post 5,318–5,084 BCE configuration; (b) E3_Tod (between 5,317 and 3,372 BCE), the top of unit 6 is displaced by synthetic and antithetic splays of the main fault; (c) after E3_Tod the top of unit 6 is reshaped by erosional events; (d) between 3468–3561 and 928–810 BCE unit 5 is deposited; (e) E2_Tod (between 913 BCE and 702 CE) unit 5 and 6 are displaced by the main fault and its antithetic splay and dragged by the main fault. The top of unit 5 is reshaped by erosional events; (f) after E2_Tod (between 668 and 874 CE) the colluvial wedge corresponding to unit 4 is deposited; (g) MRE_Tod (between 702 and 1,470 CE) caused the dragging of unit 4, 5, and 6 and the opening of a fissure; (h) After MRE_Tod and close to the 1,408–1,460 CE the fissure is infilled and the colluvial wedge corresponding to unit 3 is deposited; (i) Around 1,490–1,656 CE unit 2 is deposited; and (j) nowadays configuration.

At the Todari roadcut site the total amount of displacement of 1.05 m accumulated after 5,318–5,084 BCE (formation of unit 6), provides an average post-5 ka slip rate of 0.14–0.15 mm/yr for this secondary strand.

At the Anghiari trench site A, the presence of the gravitational sliding surface makes it difficult to measure a reliable displacement. A minimum of 1.75 m of displacement accumulated from 3,351 to 3,096 BCE, estimated by means of the base of the unit 4b (sample TA_C8, assuming a small amount of motion of the sliding. With this assumption, the calculated slip rate is 0.35 mm/yr.

5.4. Interpretation of Secondary Features

In the following we discuss a number of points that collectively support an earthquake-induced origin of the observed secondary features (Figure 8) under the current extensional stress regime.

Hydrofracturing due to pressurized fluids seems to be the most plausible mechanism for explaining the pervasive occurrence of fractures and fissures. High fluid pressure would have caused the opening of fractures, and fluid circulation probably led to the formation of bleaching halos. Fissures infilled by gray clay from unit 10 indicate that this clay was fluidized, probably due to a combination of poor lithification and high content of water at elevated pressure. The upward direction of fluid escape is indicated by the symmetry of flame and injection structures observed at the top of unit 9 (Figure 8). Moreover, the number of fractures and clay-filled fissures reduce drastically passing from unit 9 to unit 8. This suggests that the clayey paleosol of unit 8 behaved as a cap to upward-directed fluid flow. Different types of soft-sediment deformation in clayey material, generally associated with high hydraulic pressure, were documented in different geologic contexts (e.g., Van Loon, 2009 and references therein), including clay-rich clastic dykes and sills injected due to seismic-induced hydrofracturing and fluidization (e.g., Levi et al., 2006; Montenat et al., 2007).

The breccia layer at the top of unit 9 suggests mixing of material from units 9 and 8. Soft-sediment folding of different intensity, in places further deformed into mixed breccia layers, were documented in the Dead See graben (Marco et al., 1996), and are explained with mechanisms of Kelvin–Helmholtz instability due to layer-parallel shear during earthquake shaking (Heifetz et al., 2005). If the shear is unidirectional, such as for gravitational sliding along a sloping surface, folds are asymmetric. In the Villa Sterpeto trench, there are only symmetric flame structures and breccia, suggesting relative shear between the two layers sufficiently intense to produce brecciation and mixing, but not unidirectional. Back and forth displacement due to cyclic shear stress during seismic shaking can be the source of shear energy. The boundary between units 9 and 10 has no evidence of mixing and brecciation. It is very sharp, resembling a shear surface rather than a stratigraphic contact. This could be explained considering relative sliding between two units which are decoupled one from the other along a very weak interface. In other words, seismic shaking would have determined relative displacement, but because of the fluidization of clay within unit 10, the two units were completely decoupled, producing localized shear along the stratigraphic interface. This sharp boundary might appear in conflict with the observation that material from unit 10 intruded into the overlying unit 9, forming clay-filled fissures. Nevertheless, this could be explained if relative shear overprints clay injection, also during the same deformation event when fluidization, clay injection and relative shear are semi-contemporaneous.

The conjugate fissures observed in map view (Figure 8d) may suggest, at first glance, a tectonic origin under strike-slip regime. The fissures have significant opening and form a conjugate system, suggesting hybrid extensional shear fractures (e.g., Sibson, 1998) under horizontal $\sigma 1$ bisecting the acute angle and vertical $\sigma 2$. Nevertheless, a regional-scale strike-slip stress regime is unlikely for explaining the observed fissures, for three reasons: (a) the main tectonic feature in the trench is a NE-dipping normal fault; (b) AMS results (Section 4.2.4) are consistent with NE-trending extensional stress; and (c) fractures and fissures are not localized in a fault zone, but are pervasively distributed within the sedimentary layers, suggesting volumetric deformation. Cyclic shear stress due to seismic shaking might have determined deviatoric stresses within the sheared layer, with local, temporary sub-horizontal $\sigma 1$ that, in combination with high fluid pressure, would have originated conjugate sets of hybrid extensional shear fractures.

Different events of fracturing and fissuring occurred in the site, as testified by thoroughgoing fissures that cut previously formed fissures and breccia layers. This evidence of recurrent events, together with the above considerations on the possible occurrence of shaking-induced shear stress within the sedimentary layers, suggest an earthquake-induced origin for the soft-sediment deformation. The causative earthquakes should

Table 4
Expected Value of Max Magnitude (M_{max}), Average Displacement (AD) and Maximum Displacement (MD) for Two Rupture Scenarios Involving the Anghiari Fault or the Whole Anghiari-Città di Castello Main Fault, According to the Empirical Relations by Wells and Coppersmith (1994) Normal Fault and All Kinematics (WC94N and WC94 All), Leonard (2014) Deep Slip (L14 DS) and Galli et al. (2008) (G08)

Rupture scenario	Length (km)	M_{max}					AD (m)			MD (m)			W (km)		
		WC94N	WC94 all	L14 DS	G08	Average	WC94N	WC94 all	L14 DS	WC94N	WC94 all	L14 DS	WC94N	WC94 all	L14 DS
Anghiari Fault	12	6.28	6.33	6.27	6.13	6.25	0.32	0.37	0.5	0.49	0.54	0.91	11.47	10.38	8.62
Anghiari-Città di Castello main fault	25.5	6.72	6.71	6.79	6.63	6.71	0.60	0.68	0.91	1.20	1.11	1.67	16.25	13.73	14.17

have nucleated not very far from the site, as suggested by the dependency of the occurrence of liquefaction features with epicentral distance (e.g., Galli, 2000). Possibly, the earthquakes nucleated on the Anghiari normal fault, or on one of the Sansepolcro basin system faults. The earthquakes should be relatively old, when sediments were soft and below the water table, not in the present morphologic setting. Those ancient events occurred before tilting, as the fissures are tilted with the hosting sedimentary layers. Moreover, despite the tilting, the 70°-striking fissures remained subvertical (see stereonet in Figure 6), indicating that rotation occurred around an axis nearly orthogonal to that direction, which is nearly parallel to the strike of the Anghiari normal fault. This suggests that tilting is linked to progressive slip on the Anghiari fault. In summary, the secondary features observed in the Villa Sterpeto trench suggest that the site was affected by (a) pervasive soft-sediment deformation under conditions of upward-directed pressurized fluids; (b) differential bedding-parallel shear, with effects at the boundary between units with different rheologies causing mixing or localized shear; (c) superposition of different consecutive deformation events; (d) shaking-induced shear stress due to strong earthquakes on the Sansepolcro basin fault system as the most plausible mechanism for their formation; and (e) progressive tilting in the hanging wall of the Anghiari normal fault.

5.5. Seismogenic Potential and Average Extensional Rate in the Sansepolcro Basin

We calculated the expected maximum magnitude (M_{max}) from the mapped fault length using empirical regressions (Galli et al., 2008; Leonard, 2014; Wells & Coppersmith, 1994). From the obtained Mmax we derived the expected average (AD) and maximum displacement (MD). These values, summarized in Table 4, refer to two different rupture scenarios: S1) a rupture scenario which involves only the Anghiari fault (from the northern tip of the Micciano section to the southern tip of the Fighille section, total length ~12 km); S2) a rupture scenario which involves the whole Anghiari-Città di Castello main fault (total length ~25.5 km).

On average, the maximum expected magnitude derived from different empirical regressions ranges from 6.2 to 6.7 depending on the scenario. The displacements per event measured in the trenches (≥0.45 m estimated from the thickness of the wedges in the Villa Sterpeto trench and 0.18–0.52 m at the Todari roadcut) are comparable with the average displacement expected for S1 and are smaller, but not very different from the average displacement expected for S2. The values of displacement estimated from the wedges in the Villa Sterpeto trench (≥0.45 m) and the displacement related to E2_Tod (0.52 m) are also comparable with the expected maximum displacement for S1. This is consistent with the observation that the trenches are located in the zone with the greatest morphological expression along the Micciano fault section. The data collected studying in depth the Anghiari fault can be used to sensibly improve the seismic hazard assessment in the Sansepolcro basin. In fact, the fault parameters obtained with paleoseismological investigations are fundamental for fault-based seismic hazard assessments, especially where only a few macroseismic information are available from historical catalogs.

A key component in fault-based seismic hazard assessment is the slip rate. Our study provides slip rates based on chronologically constrained Late Quaternary - Holocene offsets. Nevertheless, some doubts arise when comparing the paleoseismological slip rates with the extensional rates from geodetic data. Anderlini et al. (2016) calculated GPS extension rates of ~2 mm/yr along a transect located ~30 km SE of the center of the Sansepolcro basin (across the Ponte Pattoli—Gubbio basins, see Figure 1). In the Sansepolcro basin the extension is probably less than 2 mm/yr, as extension rate along the Apennines is known to decrease to the NW (Anderlini et al., 2016; Bennett et al., 2012; D'Agostino, 2014; D'Agostino et al., 2009). For example, in D'Agostino (2014) the strain rate across the central Sansepolcro basin (12–25 nstrain/yr) is ~40% less than the strain rate across the Ponte Pattoli—Gubbio basins (27–35 nstrain/yr). Therefore, the extension rate across the Sansepolcro basin can be estimated to be between 1.5 and 2.0 mm/yr. Even considering the highest calculated paleoseismological slip rate (0.35 mm/yr), the corresponding horizontal extension for an average fault dip of 45° (the Anghiari fault up to 3 km-depth) would be ~0.25 mm/yr, which is ~⅙ of the minimum estimated GPS extension. Assuming that a comparable amount of extension is accommodated by the Sansepolcro antithetic fault, there is still ~1 mm/yr of GPS extension to be explained. This suggests one or probably a combination of the following:

- a large part of the geodetic extension is accommodated by distributed deformation between major faults, not detectable by classical geologic investigations;

- we underestimate the slip rate as we possibly missed some secondary splaying faults and/or missed the sites of maximum displacement on the Anghiari fault;
- other splays of the ATF, such as the Sovara synthetic splay, accommodate part of the extension.

A work aimed at estimating the slip rate of the fault system systematically and at a wider scale, also using geologic and geomorphic markers covering a time range wider than that constrained in this work can help a better understanding of the extensional rate of the basin during its recent evolution.

5.6. Potential Implications for Activity and Seismogenic Behavior of a Continental LANF

The evidence of surface faulting earthquakes along the Anghiari fault has potential implications in our understanding of the present activity and the seismogenic behavior of LANFs. The Anghiari fault is considered as the easternmost active synthetic splay of the ATF LANF by some authors (e.g., Barchi et al., 1998a; Bonini et al., 2016; Brozzetti et al., 2009; Pucci et al., 2014). The present activity of the ATF LANF was inferred mostly on the basis of microseismicity recorded SE of the Upper Tiber River valley, combined with seismic reflection data (Chiaraluce et al., 2007). The creeping versus seismogenic behavior, and the link with the Anghiari fault are two major issues to address about the ATF LANF.

Although the frictional fault reactivation theory predicts that slip on LANF is extremely unlikely (Collettini, 2011), the ATF capacity to source moderate to strong earthquakes (i.e., Mw $\geq$ 6) has been inferred from regional seismotectonic considerations. Brozzetti et al. (2009) claimed that the southern sector of the UTV (SSE of Città di Castello) is characterized by creeping, as suggested by the intense microseismicity and the lack of historical strong earthquakes, while the northern sector (the Sansepolcro basin) is characterized by a seismogenic behavior, as suggested by the occurrence of strong historical earthquakes. High-resolution seismologic and geodetic data documented mixed-mode (seismic and aseismic) slip behavior along the ATF (Anderlini et al., 2016; Valoroso et al., 2017) and swarm-like events on its high-angle splay faults (Gualandi et al., 2017). Particularly, according to geodetic data, Anderlini et al. (2016) argue that the ATF LANF shows both locked and creeping patches, in agreement with the possibility to nucleate strong earthquakes in the Sansepolcro basin.

To address the issue of the link with the Anghiari fault, first we have to reconcile the ground surface observations and the deep model of this low-angle fault. At the surface, the Anghiari fault does not dip at low-angle. The dip is 48°–60° in the Villa Sterpeto trench, from 40° to 74° in the Podere Todari road cut, and 46° and 70°–80° (two synthetic splays) in the Anghiari trench (site A). In high-resolution shallow seismic reflection profiles, the fault dips ∼53° up to depths of ∼40 m (Micciano section, Villa Sterpeto site, Figure 5) and ∼51° up to depths of ∼300 m (Anghiari-Motina section, Delle Donne et al., 2007). There are two possible interpretations for the relationship between the ATF LANF and the Anghiari fault:

1. the Anghiari fault dips steeply in the near-surface and becomes progressively less inclined at depth, soling into the ATF LANF at depths of 3–4 km as indicated in section A-A' of Figure 1 (from Brozzetti et al., 2009);
2. the Anghiari fault dips steeply across the entire brittle crust and offset the ATF LANF.

The first option follows the classical model of LANF, and the second one is not yet supported by data. Such information would require additional investigations. There is no high-resolution geophysical data that can image with sufficient detail the fault intersection in the 3–5 km-depth interval, and there is no detailed aftershock data of earthquakes sufficiently large to illuminate an appreciable size of the Anghiari fault.

Field observations do not allow us to discriminate between these two hypotheses. The sedimentary succession in the hanging wall of the Anghiari fault is tilted against the fault and the tilting decreases from older to younger sediments (up to 30° the CTA beds; 5°–15° the MTC beds, <5° the bottom of Late Pleistocene colluvium; Figures 3 and 6). Moreover, the CTA beds are tilted in the footwall of the Anghiari fault (Figures S1 and S3 in Supporting Information S1), suggesting that the Anghiari fault cuts through an already tilted succession in the hanging wall of the Sovara parallel fault. This evidence can suggest progressive hanging wall rollover due to listric faulting (e.g., Dula, 1991) during syn-tectonic sedimentation with an extensional model of imbricated listric normal faults rejuvenating in the direction of extension and soling into the same detachment level (Wernicke & Burchfiel, 1982). On the other hand, this would also be expected in a domino style tilt block model of faulting (Leeder & Gawthorpe, 1987; Wernicke & Burchfiel, 1982) also observed

in seismic reflection data sets (Jackson et al., 2017). Only deep high-resolution seismic reflection data can solve this uncertainty.

If the Anghiari fault is detaching on the ATF LANF at depths of ∼3.5 km as in section A-A' of Figure 1, its down-dip width is ∼5 km (average dip of 45°). To generate a $M \sim 6.2$ earthquake, a rupture width of about 9–11 km is expected based on empirical relationships (Leonard, 2014; Wells & Coppersmith, 1994). This implies that at least 4–5 km of the ruptured width should be on the ∼25°-dipping ATF LANF (up to depths of 5–6 km). For a $M \sim 6.7$ earthquake, the expected width from empirical relationship is about 13–16 km. Therefore, the expected down-dip ruptured portion of the LANF is about 8–11 km, which is close to the entire 25°-dipping ramp of the LANF in section A-A' of Figure 1 (up to depths of ∼7 km).

In synthesis, field data could support an active, seismogenic behavior of the ATF LANF, especially of the youngest and easternmost NE-dipping Anghiari splay and its down-dip continuation into the low-angle (dip $\leq 25°$) detachment. But high-resolution geophysical data in the 3–5 km-depth range appears essential for solving this issue. Karlsson et al. (2021) came to similar conclusions by studying the case of the Cañada David detachment (Baja California-Mexico). They suggest that this severely misoriented LANF is capable of nucleating strong surface faulting earthquakes, as well as other well-oriented faults in the system. As a possible mechanical explanation, they propose the "keystone fault hypothesis" formulated by Fletcher et al. (2016). The severely misoriented LANF would act as a keystone fault, able to regulate slip of other faults in the system. During interseismic loading, optimally oriented faults would bleed off the excess shear stress in small slip events and creep determining continuous stress built-up on the keystone LANF until its seismogenic failure together with other high-angle faults in its hanging wall.

6. Conclusions

We revealed for the first time the slip history of the Anghiari fault, a 12 km-long normal fault considered in the literature to be a synthetic splay of a low-angle normal fault (Altotiberina LANF).

The Anghiari fault displaces Lower-Middle Pleistocene to Holocene deposits and is capable of faulting the ground surface during strong earthquakes. The magnetic susceptibility anisotropy analysis indicates a continuously active extensional stress field. Pervasive soft-sediment deformation within the tilted Pleistocene deposits suggests repeating severe ground shaking due to strong earthquakes on the Sansepolcro basin normal fault system, and progressive tilting in the hanging wall of the Anghiari normal fault.

The most recent surface faulting earthquake (MRE_Tod) is compatible with the poorly constrained 1458 earthquake, which damaged the Città di Castello and Sansepolcro towns within the Sansepolcro basin.

According to empirical regressions, the expected maximum magnitude is on average between 6.2 and 6.7, depending on the rupture scenario.

The paleoseismological slip rate of the Anghiari fault varies between 0.14 (over the last 7 ka) and 0.35 mm/yr (over the last 5 ka), depending on the considered fault section, with a mean value >0.2 mm/yr over the last 25 ka, measured in the Villa Sterpeto trench. The mean recurrence interval ranges from about 2,500 to 3,200 years, depending on the different earthquakes age hypotheses considered. The coefficient of variation of the recurrence time is between about 0.6 and 0.9, suggesting a non-periodic behavior. If the Anghiari fault is actually the surface expression of a LANF that steepens progressively within the shallowest 3–5 km of depths and breaches the ground, our work can be among the few ones worldwide documenting the geological evidence of an active and seismogenic LANF, suggesting that earthquakes on LANFs can be less rare than previously thought. Even though only a large seismogenic rupture can solve the issue unambiguously, very high-resolution geophysics in the 3–5 km -depth interval can help to prove the connection between the paleoseismological evidence of earthquake surface faulting and the deep low-angle plane, which is challenging for future research.

Data Availability Statement

All data sets presented in this study are included in the article and in Supporting Information S1.

Acknowledgments
We are grateful to the Editor Laurent Jolivet, Zoë Mildon, and the other anonymous reviewer who have significantly improved this manuscript with their suggestions and comments. This work was funded by "Ente Acque Umbre Toscane (EAUT), Arezzo, Italy," which is warmly acknowledged (Conventions 2019 and 2020 between EAUT and Universities of Chieti—Pescara—Resp.: P. Boncio—and Perugia—Resp.: F. Mirabella, code: MIRF2019EAUT and MIRFEAUT2021). This work is also partially funded by the EQTIME ANR-project (Resp.: L. Benedetti). We wish to thank F. Florindo (INGV) for the financial support in the paleomagnetic data collection and analysis to ADC. The AMS analysis was conducted at the INGV Paleomagnetism and Environmental Magnetism Laboratory. We also thank F. Carboni and A. Akimbekova for the support during GPR data collection, M. Urbani and A. Sabatini for laser scanning of the trench in the Anghiari site A and O. Gómez Novell for support on the field and with OxCal age modelling. Finally, CNES is warmly acknowledged for providing us the Pléaides satellite images through the ISIS program. Eliana Poli and Luigi Ferranti are warmly acknowledged for their useful suggestions to the PhD thesis of AT.

References

Anderlini, L., Serpelloni, E., & Belardinelli, M. (2016). Creep and locking of a low-angle normal fault: Insights from the Altotiberina fault in the Northern Apennines (Italy). *Geophysical Research Letters*, *43*(9), 221–4329. https://doi.org/10.1002/2016GL068604

Argenti, P. (2004). Plio-Quaternary mammal fossiliferous sites of Umbria (Central Italy). *Geologica Romana*, *37*, 67–78.

Barchi, M. R. (2010). The neogene-quaternary evolution of the northern Apennines: Crustal structure, style of deformation and seismicity. In M. Beltrando, A. Peccerillo, M. Mattei, S. Conticelli, & C. Doglioni (Eds.), *The geology of Italy. Journal of virtual explorer*. https://doi.org/10.3809/jvirtex.2009.00220

Barchi, M. R., & Ciaccio, M. G. (2009). Seismic images of an extensional basin, generated at the hanging wall of a low-angle normal fault: The case of the Sansepolcro basin (Central Italy). *Tectonophysics*, *479*(3–4), 285–293. https://doi.org/10.1016/j.tecto.2009.08.024

Barchi, M. R., De Feyter, A., Magnani, M. B., Minelli, G., Pialli, G., & Sotera, B. M. (1998b). Extensional tectonics in the Northern Apennines (Italy): Evidence from the CROP03 deep seismic reflection line. *Mem. Soc. Geol. It.*, *52*, 527–538.

Barchi, M. R., Minelli, G., & Pialli, G. (1998a). The CROP 03 profile: A synthesis of results on deep structures of the northern Apennines. *Mem. Soc. Geol. It.*, *52*, 383–400.

Benedetti, L., ManigheG, I., Gaudemer, Y., Finkel, R., Malavieille, J., Pou, K., et al. (2013). Earthquake synchrony and clustering on Fucino faults (Central Italy) as revealed from in situ ^{36}Cl exposure dating. *Journal of Geophysical Research: Solid Earth*, *118*(9), 4948–4974. https://doi.org/10.1002/jgrb.50299

Bennett, R. A., Serpelloni, E., Hreinsdóttir, S., Brandon, M. T., Buble, G., Basic, T., et al. (2012). Syn-convergent extension observed using the RETREAT GPS network, northern Apennines, Italy. *Journal of Geophysical Research*, *117*(B4), B04408. https://doi.org/10.1029/2011JB008744

Benvenuti, M., Bonini, M., & Moroni, A. (2016). Tectonic control on the late quaternary hydrography of the upper Tiber basin (northern Apennines, Italy). *Geomorphology*, *269*, 85–103. https://doi.org/10.1016/j.geomorph.2016.06.017

Blumetti, A., Grutzner, C., Guerrieri, L., & Livio, F. (2017). Quaternary earthquakes: Geology and palaeoseismology for seismic hazard assessment. *Quaternary International*, *451*, 1–10. https://doi.org/10.1016/j.quaint.2017.04.002

Boncio, P., Brozzetti, F., & Lavecchia, G. (2000). Architecture and seismotectonic of a regional low-angle normal fault zone in Central Italy. *Tectonics*, *19*(6), 1038–1055. https://doi.org/10.1029/2000tc900023

Bonini, M., Corti, G., Delle Donne, D., Sani, F., Piccardi, L., Vannucci, G., et al. (2016). Seismic sources and stress transfer interaction among axial normal faults and external thrust fronts in the northern Apennines (Italy): A working hypothesis based on the 1916–1920 time–space cluster of earthquakes. *Tectonophysics*, *680*, 67–89. https://doi.org/10.1016/j.tecto.2016.04.045

Borradaile, G. J. (1988). Magnetic susceptibility, petrofabrics and strain. *Tectonophysics*, *156*(1–2), 1–20. https://doi.org/10.1016/0040-1951

Borradaile, G. J., & Henry, B. (1997). Tectonic applications of magnetic susceptibility and its anisotropy. *Earth-Science Reviews*, *42*(1–2), 49–93. https://doi.org/10.1016/S0012-8252

Borradaile, G. J., & Jackson, M. (2004). Anisotropy of magnetic susceptibility (AMS): Magnetic petrofabrics of deformed rocks. In F. Marti´n-Herna´ndez, C. Lu¨neburg, C. Aubourg, & M. Jackson (Eds.), *Magnetic Fabric methods and applications* (Vol. 238, pp. 299–360). Geol Soc Lond Spec Publ.

Bronk Ramsey, C. (1995). Radiocarbon calibration and analysis of stratigraphy. *The OxCal Program Radiocarbon*, *37*(2), 425–430. https://doi.org/10.1017/s0033822200030903

Bronk Ramsey, C. (2008). Deposition models for chronological records. *Quaternary Science Reviews*, *27*(1–2), 42–60. https://doi.org/10.1016/j.quascirev.2007.01.019

Bronk Ramsey, C. (2009). Bayesian analysis of radiocarbon dates. *Radiocarbon*, *51*(1), 337–360. https://doi.org/10.1017/S0033822200033865

Brozzetti, F., Boncio, P., Lavecchia, G., & Pace, B. (2009). Present activity and seismogenic potential of a low-angle normal fault system (Cittá di Castello, Italy): Constraints from surface geology, seismic reflection data and seismicity. *Tectonophysics*, *463*(1–4), 31–46. https://doi.org/10.1016/j.tecto.2008.09.023

Caciagli, M., Pucci, S., Batlló, J., Cesca, S., & Braun, T. (2019). Did the deadly 1917 Monterchi earthquake occur on the low-Angle Alto Tiberina (Central Italy) normal fault? *Seismological Research Letters*, *90*(3), 1131–1144. https://doi.org/10.1785/0220180155

Caricchi, C., Aldega, L., Barchi, M. R., Corrado, S., Grigo, D., Mirabella, F., & Zattin, M. (2015). Exhumation patterns along shallow low-angle normal faults: An example from the Altotiberina active fault system (northern Apennines, Italy). *Terra Nova*, *27*(4), 312–321. https://doi.org/10.1111/ter.12163

Cattuto, C., Cencetti, C., Fisauli, M., & Gregori, L. (1995). I bacini Pleistocenici di Anghiari e Sansepolcro nell'alta valle del Tevere. *Il Quaternario*, *8*, 119–128.

Chiaraluce, L., Amato, A., Carannante, S., Castelli, V., Cattaneo, M., Cocco, M., et al. (2014). The Alto Tiberina Near Fault Observatory (northern Apennines, Italy). *Annals of Geophysics*, *57*(3). https://doi.org/10.4401/ag-6426

Chiaraluce, L., Chiarabba, C., Collettini, C., Piccinini, D., & Cocco, M. (2007). Architecture and mechanics of an active low-angle normal fault: Alto Tiberina fault, northern Apennines, Italy. *Journal of Geophysical Research*, *112*(B10), B10310. https://doi.org/10.1029/2007jb005015

Ciangherotti, A., & Esu, D. (2000). Paleoecologic and biochronologic meaning of the early Pleistocene molluscan fauna from the Anghiari basin (Tiber River upper valley, central Italy). *Bollettino della Societa Paleontologica Italiana*, *39*(2), 217–224.

Cinti, F. R., Pauselli, C., Livio, F., Ercoli, M., Brunori, C. A., Ferrario, F., et al. (2015). Integrating multidisciplinary, multi-scale geological and geophysical data to image the Castrovillari fault (Northern Calabria, Italy). *Geophysical Supplements to the Monthly Notices of the Royal Astronomical Society*, *203*(3), 1847–1863. https://doi.org/10.1093/gji/ggv404

Collettini, C. (2011). The mechanical paradox of low-angle normal faults: Current understanding and open questions. *Tectonophysics*, *510*(3–4), 253–268. https://doi.org/10.1016/j.tecto.2011.07.015

Cowie, P. A., Phillips, R. J., Roberts, G. P., McCaffrey, K., Zijerveld, L. J. J., Gregory, L. C., et al. (2017). Orogen-scale uplift in the central Italian Apennines drives episodic behaviour of earthquake faults. *Scientific Reports*, *7*, 1–10. https://doi.org/10.1038/srep44858

D'Agostino, N. (2014). Complete seismic release of tectonic strain and earthquake recurrence in the Apennines (Italy). *Geophysical Research Letters*, *41*(4), 1155–1162. https://doi.org/10.1002/2014gl059230

D'Agostino, N., Mantenuto, S., D'Anastasio, E., Avallone, A., Selvaggi, G., Barchi, M., et al. (2009). Contemporary crustal extension in the Umbria-Marche Apennines from regional CGPS networks and comparison between geodetic and seismic deformation. *Tectonophysics*, *476*(1–2), 3–12. https://doi.org/10.1016/j.tecto.2008.09.033

Delle Donne, D., Piccardi, L., Odum, J. K., Stephenson, W. J., & Williams, R. A. (2007). High-resolution shallow reflection seismic image and surface evidence of the Upper Tiber Basin active faults (Northern Apennines, Italy). *Bollettino della Societa Geologica Italiana*, *126*(2), 323–331.

Dula, W. F. (1991). Geometric models of listric normal faults and rollover folds. *AAPG Bulletin*, *75*, 1609–1625. https://doi.org/10.1306/0C9B29B1-1710-11D7-8645000102C1865D

Ellsworth, W. L., Matthews, M. V., Nadeau, R. M., Nishenko, S. P., Reasen- berg, P. A., & Simpson, R. W. (1999). A physically based earthquake recurrence model for estimation of long-term earthquake probabilities. *Open-File Report - U. S. Geological Survey*, 99–522.

Ercoli, M., Bizzarri, R., Baldanza, A., Bertinelli, A., Mercantili, D., & Pauselli, C. (2021a). GPR detection of fossil structures in conductive media supported by FDTD modelling and attributes analysis: An example from early Pleistocene marine clay at Bargiano site (Central Italy). *Geosciences*, *11*(9), 386. https://doi.org/10.3390/geosciences11090386

Ercoli, M., Cirillo, D., Pauselli, C., Jol, H. M., & Brozzetti, F. (2021b). Ground-penetrating radar signature of quaternary faulting: A study from the Mt. Pollino region. southern Apennines, Italy. *Solid Earth*, *12*(11), 2573–2596. https://doi.org/10.5194/se-12-2573-2021

Ercoli, M., Pauselli, C., Cinti, F. R., Forte, E., & Volpe, R. (2015). Imaging of an active fault: Comparison between 3D GPR data and outcrops at the Castrovillari fault, Calabria, Italy. *Interpretation*, *3*, SY57–SY66. https://doi.org/10.1190/int-2014-0234.1

Ercoli, M., Pauselli, C., Frigeri, A., Forte, E., & Costanzo, F. (2013). "Geophysical paleoseismology" through high resolution GPR data: A case of shallow faulting imaging in Central Italy. *Journal of Applied Geophysics*, *90*, 27–40. https://doi.org/10.1016/j.jappgeo.2012.12.001

Field, E. H., Biasi, G. P., Bird, P., Dawson, T. E., Felzer, K. R., Jackson, D. D., et al. (2015). Long-term time-dependent probabilities for the third uniform California earthquake rupture forecast (UCERF3). *Bulletin of the Seismological Society of America*, *105*(2A), 511–543. https://doi.org/10.1785/0120140093

Fletcher, J., Oskin, M., & Teran, O. (2016). The role of a keystone fault in triggering the complex El Mayor–Cucapah earthquake rupture. *Nature Geoscience*, *9*(4), 303–307. https://doi.org/10.1038/ngeo2660

Forte, E., Pipan, M., Casabianca, D., Di Cuia, R., & Riva, A. (2012). Imaging and characterization of a carbonate hydrocarbon reservoir analogue using GPR attributes. *Journal of Applied Geophysics*, *81*, 76–87. https://doi.org/10.1016/j.jappgeo.2011.09.009

Galli, P. (2000). New empirical relationships between magnitude and distance for liquefaction. *Tectonophysics*, *324*(3), 169–187. https://doi.org/10.1016/S0040-1951(00)00118-9

Galli, P., Galadini, F., & Pantosti, D. (2008). Twenty years of paleoseismology in Italy. *Earth-Science Reviews*, *88*(1–2), 89–117. https://doi.org/10.1016/j.Earscirev.2008.01.001

Gualandi, A., Nichele, C., Serpelloni, E., Chiaraluce, L., Anderlini, L., Latorre, D., et al. (2017). Aseismic deformation associated with an earthquake swarm in the northern Apennines (Italy). *Geophysical Research Letters*, *44*(15), 7706–7714. https://doi.org/10.1002/2017GL073687

Heifetz, E., Agnon, A., & Marco, S. (2005). Soft sediment deformation by Kelvin Helmholtz instability: A case 1314 from Dead Sea earthquakes. *Earth and Planetary Science Letters*, *236*(1–2), 497–504. https://doi.org/10.1016/j.epsl.2005.04.019

Hreinsdóttir, S., & Bennett, R. A. (2009). Active aseismic creep on the Alto Tiberina low-angle normal fault, Italy. *Geology*, *37*(8), 683–686. https://doi.org/10.1130/G30194A.1

Hrouda, F. (1982). Magnetic anisotropy of rocks and its application in geology and geophysics. *Surveys in Geophysics*, *5*(1), 37–82. https://doi.org/10.1007/BF01450244

ISPRA. (2011). *Carta geologica d'Italia alla scala 1:50.0000, F. 289 Città di Castello*. ISPRA.

Jackson, C. A.-L., Bell, R. E., Rotevatn, A., & Tvedt, A. B. M. (2017). Techniques to determine the kinematics of synsedimentary normal faults and implications for fault growth models. *Geological Society, London, Special Publications*, *439*(1), 187–217. https://doi.org/10.1144/SP439.22

Karlsson, K. W., Rockwell, T. K., Fletcher, J. M., Figueiredo, P. M., Cambron, J. F., Gontz, A. M., et al. (2021). Large holocene ruptures on the Cañada David detachment, Baja California, Mexico; implications for the seismogenesis of low-angle normal faults. *Earth and Planetary Science Letters*, *570*, 117070. https://doi.org/10.1016/j.epsl.2021.117070

Lavecchia, G., Bello, S., Andrenacci, C., Cirillo, D., Ferrarini, F., Vicentini, N., et al. (2022). Quaternary fault strain INdicators database-QUIN 1.0-first release from the Apennines of central Italy. *Scientific Data*, *9*(1), 1–16. https://doi.org/10.1038/s41597-022-01311-8

Leeder, M. R., & Gawthorpe, R. L. (1987). Sedimentary models for extensional tilt-block/halfgraben basins. *Geological Society, London, Special PublicaAons*, *28*(1), 139–152. https://doi.org/10.1144/GSL.SP.1987.028.01.11

Leonard, M. (2014). Self-consistent earthquake fault-scaling relations: Update and extension to stable continental strike-slip faults. *Bulletin of the Seismological Society of America*, *104*(6), 2953–2965. https://doi.org/10.1785/0120140087

Levi, T., Weinberger, R., Aïfa, T., Eyal, Y., & Marco, S. (2006). Injection mechanism of clay-rich sediments into dikes during earthquakes. *Geochemistry, Geophysics, Geosystems*, *7*(12), Q12009. https://doi.org/10.1029/2006GC001410

Maffione, M., Pucci, S., Sagnotti, L., & Speranza, F. (2012). Magnetic fabric of Pleistocene continental clays from the hanging-wall of an active low-angle normal fault (Altotiberina Fault, Italy). *International Journal of Earth Sciences*, *101*(3), 849–861. https://doi.org/10.1007/s00531-011-0704-9

Mantenuto, S. (2008). *The active deformation in the central-northern Apennines (Abruzzo and Umbria-Marche region, Italy) through the analysis of GPS data* (PhD thesis). (p. 156). University of Perugia.

Marco, S., Stein, M., Agnon, A., & Ron, H. (1996). Long term earthquake clustering: A 50,000-year paleoseismological record in the Dead Sea graben. *Journal of Geophysical Research*, *101*(B3), 6179–6192. https://doi.org/10.1029/95JB01587C

Martini, I., Sagri, M., & Colella, A. (2001). Neogene-Quaternary basins of the inner Apennines and Calabria arc. In I. Martini (Ed.), *Anatomy of an orogen - The Apennines and adjacent Mediterranean basins* (pp. 375–400). Kluwer Academic Publisher.

Masini, F., & Sala, B. (2007). Large- and small-mammal distribution patterns and chronostratigraphic boundaries from the Late Pliocene to the Middle Pleistocene of the Italian peninsula. *Quaternary International*, *160*(1), 43–56. https://doi.org/10.1016/j.quaint.2006.09.008

McCalpin, J. P. (Ed.) (2009). Paleoseismology. *International geophysics series* (2nd ed., Vol. 95). Academic Press, Elsevier.

Mildon, Z. K., Roberts, G. P., Faure Walker, J. P., Beck, J., Papanikolaou, I., Michetti, A. M., et al. (2022). Surface faulting earthquake clustering controlled by fault and shear-zone interactions. *Nature Communications*, *13*(1), 7126. https://doi.org/10.1038/s41467-022-34821-5

Mirabella, F., Brozzetti, F., Lupattelli, A., & Barchi, M. R. (2011). Tectonic evolution of a low angle extensional fault system from restored cross sections in the northern Apennines (Italy). *Tectonics*, *30*(6), TC6002. https://doi.org/10.1029/2011tc002890

Mirabella, F., Ciaccio, M. G., Barchi, M. R., & Merlini, S. (2004). The Gubbio normal fault (Central Italy): Geometry, displacement distribution and tectonic evolution. *Journal of Structural Geology*, *26*(12), 2233–2249. https://doi.org/10.1016/j.jsg.2004.06.009

Montenat, C., Barrier, P., Ott d'Estevou, P., & Hibsch, C. (2007). Seismites: An attempt at critical analysis and classification. *Sedimentary Geology*, *196*(1–4), 5–30. https://doi.org/10.1016/j.sedgeo.2006.08.004

Montone, P., & Mariucci, M. T. (2016). The new release of the Italian contemporary stress map. *Geophysical Journal International*, *205*(3), 1525–1531. https://doi.org/10.1093/gji/ggw100

Oddone, E. (1918). Il terremoto dell'alta valle del Tevere del 26 aprile 1917. *Bollettino della Società Sismologica Italiana*, *21*, 9–27.

Pace, B., Peruzza, L., Lavecchia, G., & Boncio, P. (2006). Layered seismogenic source model and probabilistic seismic-hazard analyses in central Italy. *Bulletin of the Seismological Society of America*, *96*(1), 107–132. https://doi.org/10.1785/0120040231

Pace, B., Visini, F., & Peruzza, L. (2016). *FiSH: MATLAB tools to turn fault data into seismic-hazard models*. Electronic Seismologist.

Pace, B., Visini, F., Scotti, O., & Peruzza, L. (2018). Preface: Linking faults to seismic hazard assessment in Europe. *Natural Hazards and Earth System Sciences*, *18*(5), 1349–1350. https://doi.org/10.5194/nhess-18-1349-2018

Pialli, G., Barchi, M., & Minelli, G. (1998). Results of the CROP03 deep seismic reflection profile. *Memorie della Societa Geologica Italiana*, *52*, 654.

Piccinini, D., Cattaneo, M., Chiarabba, C., Chiaraluce, L., De Martin, M., Di Bona, M., et al. (2003). A microseismic study in a low seismicity area of Italy: The Citta di Castello 2000 e 2001 experiment. *Annales Geophysicae*, *46*(6), 1315e1324.

Pondrelli, S. (2002). European-Mediterranean regional centroid-moment tensors catalog (RCMT) [Dataset]. Retrieved from https://api.semanticscholar.org/CorpusID:129482481

Pucci, S., Mirabella, F., Pazzaglia, F., Barchi, M. R., Melelli, L., Tuccimei, P., et al. (2014). Interaction between regional and local tectonic forcing along a complex Quaternary extensional basin: Upper Tiber Valley, Northern Apennines, Italy. *Quaternary Science Reviews*, *102*, 111–132. https://doi.org/10.1016/j.quascirev.2014.08.009

Reimer, P. J., Austin, W. E. N., Bard, E., Bayliss, A., Blackwell, P. G., Bronk Ramsey, C., et al. (2020). The IntCal20 northern Hemisphere radiocarbon age calibration Curve (0-55 cal kBP). *Radiocarbon*, *62*(4), 725–757. https://doi.org/10.1017/RDC.2020.41

Rockwell, T. K., Meltzner, A. J., Haaker, E. C., & Madugo, D. (2022). The late Holocene history of Lake Cahuilla: Two thousand years of repeated fillings within the Salton trough, Imperial Valley, California. *Quaternary Science Reviews*, *282*, 107456. https://doi.org/10.1016/j.quascirev.2022.107456

Rovida, A., Locati, M., Camassi, R., Lolli, B., Gasperini, P., & Antonucci, A. (2022). *Catalogo Parametrico dei Terremoti Italiani (CPTI15), versione 4.0*. Istituto Nazionale di Geofisica e Vulcanologia (INGV). https://doi.org/10.13127/CPTI/CPTI15.4

Sani, F., Bonini, M., Piccardi, L., Vannucci, G., Delle Donne, D., Benvenuti, M., et al. (2009). Late Pliocene–Quaternary evolution of outermost hinterland basins of the Northern Apennines (Italy), and their relevance to active tectonics. *Tectonophysics*, *476*(1–2), 336–356. https://doi.org/10.1016/j.tecto.2008.12.012

Schlagenhauf, A., Manighe, G. I., Benede, G. L., Gaudemer, Y., Finkel, R., Malavieille, J., & Pou, K. (2011). Earthquake supercycles in Central Italy, inferred from ^{36}Cl exposure dating. *Earth and Planetary Science Letters*, *307*(3–4), 487–500. https://doi.org/10.1016/j.epsl.2011.05.022

Scotti, O., Visini, F., Faure Walker, J., Peruzza, L., Pace, B., Benedetti, L., et al. (2021). Which Fault threatens Me most? Bridging the gap between geologic data-providers and seismic risk practitioners. *Frontiers in Earth Science*, *8*, 626401. https://doi.org/10.3389/feart.2020.626401

Serpelloni, E., Anzidei, M., Baldi, P., Casula, G., & Galvani, A. (2005). Crustal velocity and strain-rate fields in Italy and surrounding regions: New results from the analysis of permanent and ISPRA non-permanent GPS networks. *Geophysical Journal International*, *161*(3), 861–880. https://doi.org/10.1111/j.1365-246X.2005.02618.x

Sibson, R. H. (1998). Brittle failure mode plots for compressional and extensional tectonic regimes. *Journal of Structural Geology*, *20*(5), 655–660. https://doi.org/10.1016/S0191-8141(98)00116-3

Taner, M. T., Koehler, F., & Sheriff, R. E. (1979). Complex seismic trace analysis. *Geophysics*, *44*(6), 1041–1063. https://doi.org/10.1190/1.1440994

Tarling, D. H., & Hrouda, F. (1993). *The magnetic anisotropy of rocks*. Chapman and Hall.

Tarquini, S., Vinci, S., Favalli, M., Doumaz, F., Fornaciai, A., & Nannipieri, L. (2012). Release of a 10-m-resolution DEM for the Italian territory: Comparison with global-coverage DEMs and anaglyph-mode exploration via the web. *Computers & Geosciences*, *38*(1), 168–170. https://doi.org/10.1016/j.cageo.2011.04.018

Testa, A., Valentini, A., Boncio, P., Pace, B., Visini, F., Mirabella, F., & Pauselli, C. (2021). Probabilistic fault displacement hazard analysis of the Anghiari - Città di Castello normal fault (Italy). *Italian Journal of Geosciences*, *140*(3), 327–346. https://doi.org/10.3301/IJG.2021.07

Valentini, A., Fukushima, Y., Contri, P., Ono, M., Sakai, T., Thompson, S., et al. (2021). Probabilistic fault displacement hazard assessment for nuclear installations according to IAEA safety standards. *Bulletin of the Seismological Society of America*, *111*(5), 2661–2672. https://doi.org/10.1785/0120210083

Valoroso, L., Chiaraluce, L., Di Stefano, R., & Monachesi, G. (2017). Mixed-mode slip behavior of the Altotiberina low-angle normal fault system (Northern Apennines, Italy) through high-resolution earthquake locations and repeating events. *Journal of Geophysical Research: Solid Earth*, *122*(12), 10220–10240. https://doi.org/10.1002/2017JB014607

Van Loon, A. J. (2009). Soft-sediment deformation structures in siliciclastic sediments: An overview. *Geologos*, *15*(1), 3–55.

Visini, F., & Pace, B. (2014). Insights on a key parameter of earthquake forecasting, the coefficient of variation of the recurrence time, using a simple earthquake simulator. *Seismological Research Letters*, *85*(3), 703–713. https://doi.org/10.1785/0220130165

Webber, S., Norton, K. P., Little, T. A., Wallace, L. M., & Elias, S. (2018). How fast can low-angle normal faults slip? Insights from cosmogenic exposure dating of the active Mai'iu fault, Papua New Guinea. *Geology*, *46*(3), 227–230. https://doi.org/10.1130/G39736.1

Wells, D. L., & Coppersmith, K. J. (1994). New empirical relationships among magnitude, rupture length, rupture width, rupture area, and surface displacement. *Bulletin of the Seismological Society of America*, *84*, 974–1002.

Wernicke, B., & Burchfiel, B. C. (1982). Modes of extension tectonics. *Journal of Structural Geology*, *4*(2), 105–115. https://doi.org/10.1016/0191-8141(82)90021-9

References From the Supporting Information

Ercoli, M., Pauselli, C., Frigeri, A., Forte, E., & Costanzo, F. (2014). 3-D GPR data analysis for high-resolution imaging of shallow subsurface faults: The Mt Vettore case study (central Apennines, Italy). *Geophysical Journal International*, *198*(1), 609–621. https://doi.org/10.1093/gji/ggu156

Jelinek, V. (1978). Statistical processing of magnetic susceptibility on groups of specimens. *Studia Geophysica et Geodaetica*, *22*(1), 50–62. https://doi.org/10.1007/bf01613632

Jol, H. M. (2009). In H. M. Jol (Ed.), *Ground penetrating radar theory and applications* (p. 524). Elsevier Science.

Palmer, D. (1980). *The generalized reciprocal method of seismic refraction interpretation* (p. 113). Society of Exploration Geophysicists.

Yilmaz, O. (2001). *Seismic data analysis: Processing, inversion, & interpretation of seismic data*. Investigations in Geophysics. No. 10 (Vol. 1–2). Society of Exploration Geophysicists.